Key Points:
- Spatially variable biocolloid attachment strongly contributes to an early time substantial increase in biocolloid spreading
- Biocolloid plume spreading and enhanced transport were shown to increase with increasing variability of the attachment coefficient
- Neglecting to account for aquifer chemical heterogeneity may lead to erroneous predictions of biocolloid transport in porous media

Correspondence to:
C. V. Chrysikopoulos,
cvc@enveng.tuc.gr

Impact of Spatially Variable Collision Efficiency on the Transport of Biocolloids in Geochemically Heterogeneous Porous Media

Vasileios E. Katzourakis[1] and Constantinos V. Chrysikopoulos[2] (iD)

[1]Environmental Engineering Laboratory, Civil Engineering Department, University of Patras, Patras, Greece, [2]School of Environmental Engineering, Technical University of Crete, Chania, Greece

Abstract The effect of spatially variable attachment coefficient on biocolloid transport in geochemically heterogeneous porous formations was investigated numerically with a newly developed three–dimensional mathematical model. The biocolloid transport model accounts for horizontal uniform flow in water saturated porous media, and assumes that the biocolloid attachment varies spatially with a constant mean and random fluctuations. Biocolloid particles can either be suspended in the aqueous phase or attached (reversibly or irreversibly) onto the solid matrix. Multiple random realizations of geochemically heterogeneous porous media were employed in order to obtain appropriate ensemble mean concentration distributions, which subsequently were used for classical moment analysis. Emphasis was given in the proper selection of the number of realizations required for the correct ensemble mean estimation of a stochastic variable. The results showed that the existence of spatially variable biocolloid attachment efficiency, caused by geochemical heterogeneity, strongly contributes to an early time substantial increase in biocolloid spreading, an effect that asymptotically dissipated when the migrating biocolloid plume had sampled all of the geochemical heterogeneity within the porous formation. Furthermore, biocolloid plume spreading and enhanced transport were shown to increase with increasing variability of the attachment coefficient. Our findings suggested that neglecting to account for aquifer chemical heterogeneity may lead to erroneous predictions of biocolloid transport in porous media.

1. Introduction

The effect of large-scale heterogeneity on the transport of conservative and reactive contaminants as well as suspended particles (colloids and biocolloids) in porous and fractured formations has been extensively investigated in the literature (Abdel-Salam & Chrysikopoulos, 1995; Chrysikopoulos & Abdel-Salam, 1997; Maghrebi et al., 2013; Saiers et al., 1994). Substantially different is the role of nano-scale heterogeneity, which has also been explored (Bradford et al., 2016; Pazmino et al., 2014). Several studies have explored the effect of spatially or temporally variable physicochemical parameters on contaminant and particle transport in water saturated porous media (Bekhit & Hassan, 2005; Chrysikopoulos & Sim, 1996; Chrysikopoulos et al., 1990a, 1992a, 1992b; Gao et al., 2013; Garabedian, 1987; Huysmans & Dassargues, 2009; Maghrebi et al., 2013; Sun et al., 2001; Valocchi, 1989) and investigated the influence of attachment rate distributions (Li et al., 2004; Tufenkji & Elimelech, 2005). However, the geochemical heterogeneity of subsurface formations has not been thoroughly examined in the literature. Furthermore, the transport of colloids and biocolloids in geochemically heterogeneous formations, where biocolloid attachment onto the solid matrix is spatially variable is still not fully understood, because it has received very little attention (Sun et al., 2001).

The adhering of biocolloid particles onto the solid matrix of porous media can be affected by blocking, straining, pore-space physical heterogeneity and solid-matrix surfaces geochemical heterogeneity (Loveland et al., 2003; Ryan & Elimelech, 1996). Geochemical heterogeneity can cause the solid-matrix surfaces to have spatially variable affinity for biocolloid attachment due to the variability in the developed electrostatic forces. Ryan et al. (1999) reported that the geochemical heterogeneity caused by ferric oxyhydroxide coated sand grains, can greatly control the transport of virus and silica colloids. Similarly, Schijven et al. (2000) observed that the migration of microorganisms could be affected by spatially varying distributions of ferric oxyhydroxide, because positively charged ferric surfaces attracted the negatively charged microorganisms.

On the other hand, dissolved organic matter (DOM) can reduce virus attachment on the pore surfaces of porous media. DOM is mainly made of humic acids, polysaccharides, polyphenols, proteins, lipids, and other organic molecules (Fujita et al., 1996; Imai et al., 2002; Ma et al., 2001). Gerba (1984) found that DOM has a tendency to compete with virus particles for attachment sites in subsurface formations. Yuan et al. (2008) reported that the deposition of bacteriophage MS2 was significantly reduced when silica grains were coated with natural organic matter (NOM), because negatively charged NOM surfaces created repulsive forces towards the negatively charged MS2.

Traditionally, the process of biocolloid attachment on the pore surfaces of porous media is modeled using colloid filtration theory (CFT) (Bales et al., 1991; Deborde et al., 1999; Kinoshita et al., 1993; Pieper et al., 1997; Redman et al., 1997; Ryan et al., 1999). CFT assumes that the particle attachment onto a collector grain is mainly controlled by the collision efficiency, which is the ratio of the successful collisions (collisions that lead to attachment) divided by the number of the total collisions between the collector grains and suspended particles (Rajagopalan & Tien, 1976; Tufenkji & Elimelech, 2004). It should be noted that repulsive and attractive forces generated by various surface charges characterize the collision efficiency. Therefore, a porous subsurface formation with geochemical heterogeneity is expected to have different collision efficiency values at different locations within the formation.

The purpose of this work was to investigate in depth the transport of biocolloid particles in a multi-dimensional, geochemically heterogeneous, water saturated formation. A novel three-dimensional mathematical model was developed, which assumes that the collision efficiency is a stochastic spatially variable parameter.

2. Mathematical Development

2.1. Transport Model

The transport of biocolloids (i.e. viruses, bacteria) in a three-dimensional, homogeneous, water saturated, porous media with developed one-directional uniform flow, accounting for a combination of non-equilibrium reversible and irreversible attachment onto the solid matrix, is governed by the following partial differential equation (Katzourakis, 2014; Katzourakis & Chrysikopoulos,, 2015):

$$\frac{\partial C_b}{\partial t} + \frac{\rho_s}{\theta}\frac{\partial C_b^*}{\partial t} = D_x\frac{\partial^2 C_b}{\partial x^2} + D_y\frac{\partial^2 C_b}{\partial y^2} + D_z\frac{\partial^2 C_b}{\partial z^2} - U_x\frac{\partial C_b}{\partial x} - \lambda_b C_b + F_b \tag{1}$$

where C_b [M_b/L^3] is the concentration of the suspended biocolloids; C_b^* [M_b/M_s] is the concentration of biocolloids attached onto the solid matrix; x [L], y [L], and z [L] are the Cartesian coordinates in the longitudinal, lateral, and vertical direction, respectively; t [t] is time; θ [–] is the porosity of the porous medium; ρ_s [M_s/L^3] is the bulk density of the solid matrix; U_x [L/t] is the average interstitial velocity along the x-direction; D_x, D_y, D_z [L^2/t] are the longitudinal, lateral, and vertical hydrodynamic dispersion coefficients of the suspended biocolloids, respectively; λ_b [1/t] is the decay rate of biocolloids suspended in the liquid phase; and F_b [$M_b/L^3 \cdot t$] is a general form of the biocolloid source configuration. For simplicity, the various masses are indicated as follows: M_b is the mass of biocolloids, and M_s is the mass of the solid matrix. The second accumulation term found on the left hand side of equation (1) is given by (Sim & Chrysikopoulos, 1998, 1999):

$$\frac{\rho_s}{\theta}\frac{\partial C_b^*}{\partial t} = r_{b-b^*}C_b - r_{b^*-b}\frac{\rho_s}{\theta}C_b^* - \lambda_b^*\frac{\rho_s}{\theta}C_b^* \tag{2}$$

where r_{b-b^*} [1/t] is the forward rate coefficient of biocolloid attachment onto the solid matrix; r_{b^*}-b [1/t] is the reverse rate coefficient of biocolloid detachment from the solid matrix, and λ_b^* [1/t] is the decay rate of biocolloids attached onto the solid matrix. The general form of the source configuration, F_b, is written as (Sim & Chrysikopoulos, 1999):

$$F_b(t, x, y, z) = G(t)W(x, y, z) \tag{3}$$

where G(t) is the mass release function of colloids, with units of [$M_b/L^3 t$] for a volume source and [M_b/t] for a point source; W(x,y,z) characterizes the source physical geometry, with units of for a volume source and [$1/L^3$] for a point source. Moreover, for a point source geometry, W(x,y,z) is written as follows:

$$W(x, y, z) = \delta(x-x_0)\delta(y-y_o)\delta(z-z_0) \tag{4}$$

where x_0, y_0, and z_0 are the Cartesian x-, y-, and z-coordinate locations of the source centre, respectively; and $\delta(x-x_0)$, $\delta(y-y_0)$, and $\delta(z-z_0)$, are modified Dirac delta functions (e.g. $\delta=1$ for $x = x_0$, $\delta=0$ for $x \neq x_0$). Furthermore, the mass release rate as broad pulse is given by:

$$G(t) = \frac{M_{mr}}{\theta} H(t) \tag{5}$$

where M_{mr} is the mass release rate, with units of $[M_b/L^3 \cdot t]$ for a volume source and $[M_b/t]$ for a point source; and $H(t)$ is the Heaviside or unit step function ($H(t < 0)=0$, $H(t \geq 0)=1$).

The initial and boundary conditions for a three-dimensional confined aquifer with finite dimensions are:

$$C_b(0, x, y, z) = 0 \tag{6}$$

$$C_b(t, 0, y, z) = 0 \tag{7}$$

$$\frac{\partial C_b^2(t, L_x, y, z)}{\partial x^2} = 0 \tag{8}$$

$$\frac{\partial C_b(t, x, 0, z)}{\partial y} = \frac{\partial C_b(t, x, L_y, z)}{\partial y} = 0 \tag{9}$$

$$\frac{\partial C_b(t, x, y, 0)}{\partial z} = \frac{\partial C_b(t, x, y, L_z)}{\partial z} = 0 \tag{10}$$

where L_x, L_y, and L_z [L] are the length, width, and height of the porous medium, respectively. The initial condition (6) describes that at the beginning of the simulation no biocolloid concentration was available within the three-dimensional aquifer. Furthermore the boundary condition (7) implies that no biocolloids are entering the porous medium from upstream (Chrysikopoulos et al., 2012). Boundary condition (8) preserves concentration "slope" continuity at downstream $x = L_x$ (Shamir & Harleman, 1967), which is slightly different than the frequently employed first derivative boundary condition that preserves concentration continuity (Chrysikopoulos et al., 1990b). Finally, conditions (9) and (10) describe that the aquifer is impermeable at the vertical and lateral directions, ensuring that there is no flux of colloids across the lateral and vertical boundaries of the confined aquifer.

2.2. Filtration Theory
The forward rate coefficient can be defined as (Sim & Chrysikopoulos, 1995):

$$r_{b-b*} = U_x \Phi F(C_b^*) \tag{11}$$

where $F(C_b^*)$ is the dynamic blocking function that takes into account porosity variations when particle attachment is increasing; Φ [1/L] is the filter coefficient; Assuming that the porous medium is "clean," for submicron particles such as viruses, it is reasonable to assume that $F(C_b^*)=1$. Consequently, equation (11) can be rewritten as:

$$r_{b-b*} = U_x \Phi \tag{12}$$

The filter coefficient Φ can be written as (Rajagopalan & Tien, 1976):

$$\Phi = \frac{3(1-\theta)}{2d_c} \eta \tag{13}$$

where d_c [L] is the average collector diameter; and η is the single collector removal efficiency, which can be written as (Yao et al., 1971):

$$\eta = \alpha \eta_o \tag{14}$$

where α is the collision efficiency; η_o is the single collector removal efficiency under favorable deposition (when double layer interactions are attractive), which is given by (Tufenkji & Elimelech, 2004):

$$\eta_o = 2.4 A_s^{1/3} N_R^{-0.081} N_{Pe}^{-0.715} N_{vdw}^{0.052} + 0.55 A_s N_R^{1.675} N_A^{0.125} + 0.22 N_R^{-0.24} N_G^{1.11} N_{vdw}^{0.053} \tag{15}$$

where A_s is the streamline parameter, a porosity dependent parameter:

$$A_s = \frac{2(1-\varepsilon_\theta^5)}{2-3\varepsilon_\theta+3\varepsilon_\theta^5-2\varepsilon_\theta^6} \tag{16}$$

where ε_θ is defined as:

$$\varepsilon_\theta = (1-\theta)^{1/3} \tag{17}$$

N_R is the relative aspect ratio:

$$N_R = \frac{d_b}{d_c} \tag{18}$$

where d_b [L] is the biocolloid particle diameter; N_{Pe} is the Peclet number:

$$N_{Pe} = \frac{d_c U_x \theta}{D} \tag{19}$$

where D [L^2/t] is the bulk diffusion coefficient:

$$D = \frac{k_B T}{3\pi \mu_w d_b} \tag{20}$$

where k_B [kg·m^2/(s^2·K)] is the Boltzman constant; T [Kelvin] is the fluid absolute temperature; N_G is the gravity number:

$$N_G = \frac{d_b^2(\rho_b-\rho_w)g}{18\mu_w U_x \theta} \tag{21}$$

where μ_w [M_b/(L·t)] is absolute water viscosity, ρ_b [M_b/L^3] is the density of the biocolloid particles, and ρ_w [M_w/L^3] is the water density; g [L/t^2] gravitational acceleration; N_{vdw} is the van der Waals number:

$$N_{vdw} = \frac{A_{123}}{k_B T} \tag{22}$$

where A_{123} [$M_b·L^2/t^2$] is the complex Hamaker constant for the interactive media (biocolloid-water-aquifer); N_A is the attraction number:

$$N_A = \frac{N_{vdw}}{N_R N_{Pe}} \tag{23}$$

2.3. Spatially Variable Collision Efficiency

Assuming that natural subsurface formations are geochemically heterogeneous (Sun et al., 2001) with different collision efficiency values at different locations within the formation, a similar approach to the one used for the description of solute sorption and retardation (Chrysikopoulos et al., 1990a) is employed in this work for colloid and biocolloid collision efficiency and attachment. Thus, the colloid and biocolloid collision efficiency is assumed to be a Gaussian or normally distributed random field (Bosma & van der Zee, 1993; Chrysikopoulos et al., 1990a; Sun et al., 2001) with expectation $E(\alpha)=\mu_\alpha$ and variance σ_α^2. Furthermore, the extent of the collision efficiency variability in relation to its mean value is measured by the dimensionless coefficient of variation, CV, defined as:

$$CV = \frac{\sigma_\alpha}{\mu_\alpha} \tag{24}$$

where σ_α is the standard deviation of the collision efficiency. Note that the coefficient of variation is also known as relative standard deviation.

A Gaussian random field can be uniquely determined from its expectation and covariance functions (Schmidt, 2015). For an anisotropic, geochemically heterogeneous, three-dimensional porous medium, the covariance function of the normally distributed collision efficiency can be expressed as (Bao et al., 2003; Sun et al., 2001):

$$Cov_\alpha(\mathbf{r}_\alpha) = \sigma_\alpha^2 \exp\left[-\left(\frac{r_{\alpha x}^2}{\zeta_{\alpha x}^2}+\frac{r_{\alpha y}^2}{\zeta_{\alpha y}^2}+\frac{r_{\alpha z}^2}{\zeta_{\alpha z}^2}\right)^{1/2}\right] \tag{25}$$

where $\mathbf{r}_\alpha = (r_{\alpha x}, r_{\alpha y}, r_{\alpha z})^\mathsf{T}$ is a three-dimensional vector whose magnitude, $|\mathbf{r}_\alpha|$, defined as:

$$|\mathbf{r}_\alpha| = \sqrt{r_{\alpha x}{}^2 + r_{\alpha y}{}^2 + r_{\alpha z}{}^2} = \sqrt{(x_1 - x_2)^2 + (y_1 - y_2)^2 + (z_1 - z_2)^2} \tag{26}$$

is the separation distance between two collision efficiency values estimated at two different points within the heterogeneous domain with coordinates (x_1, y_1, z_1) and (x_2, y_2, z_2), respectively; $\zeta_{\alpha x}$, $\zeta_{\alpha y}$ and $\zeta_{\alpha z}$ are the correlation length scales of the collision efficiency in the longitudinal, lateral, and vertical directions, respectively. For an isotropic, geochemically heterogeneous porous medium, equation (25) reduces to:

$$Cov_\alpha(\mathbf{r}_\alpha) = \sigma_\alpha^2 \exp\left[-\frac{|\mathbf{r}_\alpha|}{\zeta_\alpha} \right] \tag{27}$$

where ζ_α is the independent of direction (isotropic) correlation length scale.

3. Moment Analysis

The absolute temporal moments are given:

$$m_n^t = \int_0^\infty t^n C_b(x, y, z, t) \ dt \tag{28}$$

where the subscript n = 0, 1, 2 indicates the order of the moment at a particular location with coordinates (x,y,z). The zeroth absolute temporal moment, m_0^t [$t \cdot M_b/L^3$], is the total mass observed at a specific location. The first absolute temporal moment, m_1^t [$t^2 \cdot M_b/L^3$], describes the mean residence time of the suspended concentration plume C_b, multiplied by the zeroth temporal moment, and the second absolute temporal moment, m_2^t [$t^3 \cdot M_b/L^3$], provides information about the degree of concentration spreading. Also, the normalized temporal moments can be defined in a general form as (James & Chrysikopoulos, 2011):

$$M_n^t = \frac{m_n^t}{m_0^t} = \frac{\int_0^\infty t^n C_b(x, y, z, t) \ dt}{\int_0^\infty C_b(x, y, z, t) \ dt} \tag{29}$$

The first normalized temporal moment, M_1^t [t], describes the mean breakthrough time (residence time) or average velocity. The second normalized temporal moment, M_2^t [t^2], characterizes the temporal spreading of the concentration distribution.

The three-dimensional absolute spatial moments can be written as (Aris, 1956; Goltz & Roberts, 1987; Singha & Gorelick, 2005):

$$m_{ijk}^s = \theta \int_0^\infty \int_0^\infty \int_0^\infty x^i y^j z^k \ C_b(x, y, z, t) \ dxdydz \tag{30}$$

where the sum of the variables i + j + k = 0, 1, 2 indicate the order of the moment, and the porosity θ is assumed to be constant. The zeroth absolute spatial moment (m_{000}^s [M_b]) quantifies the total mass found in the aquifer. The first absolute spatial moment $\left(m_{100}^s, \ m_{010}^s, \ m_{001}^s \ [M_b \cdot L] \right)$ is the center of mass of the concentration distribution in each principal direction times the zeroth spatial moment. The second absolute spatial moment $\left(m_{200}^s, \ m_{020}^s, \ m_{002}^s, \ m_{110}^s, \ m_{101}^s, \ m_{011}^s \ [M_b \cdot L^2] \right)$ provides information about the degree of mass spreading in a specific direction. Also, the normalized spatial moments can be defined in a general form as:

$$M_{ijk}^s = \frac{m_{ijk}^s}{m_{000}^s} = \frac{\int_0^\infty \int_0^\infty \int_0^\infty x^i y^j z^k C_b(x, y, z, t) \ dxdydz}{\int_0^\infty \int_0^\infty \int_0^\infty C_b(x, y, z, t) \ dxdydz} \tag{31}$$

The first normalized spatial moment $\left(M_{100}^s, \ M_{010}^s, \ M_{001}^s \ [L] \right)$ represents the center of mass of the concentration distribution in each principal direction. The second normalized spatial moment $\left(M_{200}^s, \ M_{020}^s, \ M_{002}^s, \ M_{110}^s, \ M_{101}^s, \ M_{011}^s \ [L^2] \right)$ characterizes the spatial spreading of the concentration distribution. For example, the second normalized spatial moment about the center of mass defines the following spatial covariance tensor (Freyberg, 1986):

$$\mathbf{S^2} = \begin{bmatrix} S_{xx}^2 & S_{xy}^2 & S_{xz}^2 \\ S_{yx}^2 & S_{yy}^2 & S_{yz}^2 \\ S_{zx}^2 & S_{zy}^2 & S_{zz}^2 \end{bmatrix} \tag{32}$$

where

$$S_{xx}^2 = M_{200}^s - \left(M_{100}^s\right)^2, \quad S_{yy}^2 = M_{020}^s - \left(M_{010}^s\right)^2, \quad S_{zz}^2 = M_{002}^s - \left(M_{001}^s\right)^2,$$

$$S_{xy}^2 = S_{yx}^2 = M_{110}^s - M_{100}^s M_{010}^s, \quad S_{xz}^2 = S_{zx}^2 = M_{101}^s - M_{100}^s M_{001}^s, \tag{33}$$

$$S_{yz}^2 = S_{zy}^2 = M_{011}^s - M_{010}^s M_{001}^s$$

Based on the pioneering work by Aris (1956), the relationship between the dispersion coefficient tensor, $\mathbf{D}$, and the time rate of change of the spatial covariance tensor is as follows:

$$\mathbf{D} = \frac{1}{2} \frac{d}{dt} \left(\mathbf{S^2}\right) \tag{34}$$

Furthermore, the dispersion coefficient tensor is expressed as (Bear, 1972):

$$\mathbf{D} = \mathbf{A}|\mathbf{U}| + D\mathbf{I} \tag{35}$$

where $\mathbf{A}$ is the dispersivity tensor, $|\mathbf{U}|$ is the magnitude of the interstitial velocity vector, and $\mathbf{I}$ is an identity matrix. In view of equations (34) and (35) the dispersivity tensor is related to the change of the spatial covariance tensor as follows:

$$\mathbf{A} = \frac{1}{|\mathbf{U}|} \left[\frac{1}{2}\frac{d}{dt}\left(\mathbf{S^2}\right) - D\mathbf{I}\right] \tag{36}$$

4. Numerical Procedures

The mathematical model described by equations (1–10) was solved numerically with the classical finite difference approach using the implicit Crank-Nikolson scheme. The resulting large linear system of equations was handled with the Pardiso package (Schenk & Gärtner, 2004), which is a thread-safe, and memory efficient software able to solve sparse symmetric and asymmetric linear systems of equations. High performance was ensured by distributing computational load over a number of individual processors on shared-memory and distributed-memory systems. The required two-dimensional and three-dimensional random field realizations of the spatially variable collision efficiency, α, were generated with the "Gaussian process generator" Algorithm 12.1 (Schmidt, 2015). Figure 1 presents a single random field of the three-dimensional, normally distributed collision efficiency. Furthermore, the effect of CV and correlation length on two-dimensional, isotropic normally distributed collision efficiency is illustrated in Figure 2.

5. Simulations

In this study, two different, water saturated, physically homogeneous, but chemically heterogeneous (isotropic or anisotropic) aquifers, surrounded with impermeable boundaries were considered. Aquifer-I was two-dimensional with length $L_x = 30$ m and width $L_y = 15$ m. Whereas, Aquifer-II was three-dimensional with length $L_x = 6$ m, width $L_y = 3$ m and thickness $L_z = 3$ m (see Figure 3). The groundwater flow in both of the aquifers considered was assumed to be uniform (constant)
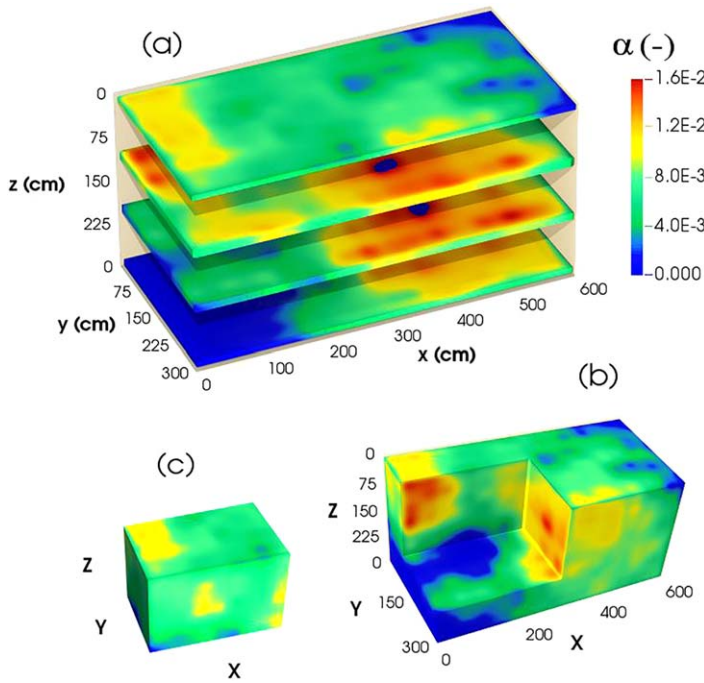
Figure 1. Single random field realization of the three-dimensional, isotropic, spatially variable collision efficiency presented as: (a) surface contours at specified horizontal (x-y plane) slices, (b) surface contour with a subtracted orthogonal core, and (c) surface contour of subtracted orthogonal core. Here $\mu_\alpha = 0.0048$, $\sigma_\alpha = 0.0081$ ($CV = \sigma_\alpha / \mu_\alpha = 170\%$), $\zeta_\alpha = 120$ cm, $L_x = 600$ cm, $L_y = 300$ cm, and $L_z = 300$ cm.
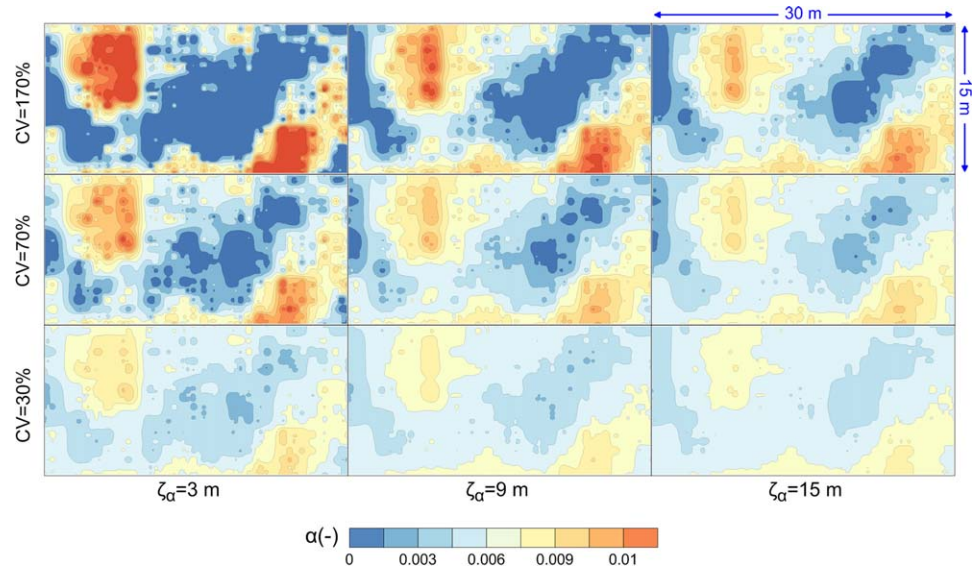
Figure 2. Random field realizations of two-dimensional, isotropic, spatially variable collision efficiency for various values of the coefficient of variation (CV) and correlation length (ζ_α). Here μ_α=0.005, L_x=30 m, L_y=15 m.

along the longitudinal direction. Furthermore, it was assumed that the aquifers consisted of quartz sand with diameter d_c=0.6 mm. Also, the migrating biocolloid was modeled after bacteriophage MS2 with diameter d_b=2.5 × 10^{-6} cm and density ρ_b =1.42 × 10^{-3} kg/cm³ (Walshe et al., 2010). The complex Hamaker constant of the interactive media (biocolloid-water-sand) was set to A_{123}=9.72 × 10^{-10} kg·cm²/h² (Murray & Parks, 1980). A representative value for the mean collision efficiency coefficient, μ_α, for viruses (bacteriophage MS2) was selected from the literature as μ_α=0.0048 (Syngouna & Chrysikopoulos, 2011), with a coefficient of variation CV = 50% (Flynn et al., 2004). Note that for μ_α=0.0048, the corresponding average attachment rate coefficient evaluated from equations (11–23) is $\mu_{r_{b-b^*}}$=0.119 1/hr. However, a different r_{b-b^*} was determined for each value of the spatially variable collision efficiency. All parameter values required for the simulations presented in this work are listed in Table 1.

It was assumed that viruses enter Aquifer-I, over a time period t_p=2,000 h, from a continuous point source located at x_0=500 cm, y_0=750 cm, based on equation (3), as follows:

$$F_v(t, x, y) = 1 \; \delta(x-500)\delta(y-750) \; \frac{mg}{mL \cdot hr} \qquad (37)$$

Also, it was assumed that viruses enter Aquifer-II, over a time period t_p=300 h, from a continuous point source located at x_0=100 cm, y_0=150 cm, and z_0=150 cm, as follows:

$$F_v(t, x, y, z) = 1 \; \delta(x-100)\delta(y-150)\delta(z-150) \; \frac{mg}{mL \cdot hr} \qquad (38)$$

The mass release function, defined by equation (5), was set to G(t)=1 mg/hr $\left(0 \leq t < t_p\right)$. Furthermore unless it is otherwise explicitly stated, the source time period for Aquifer-I and Aquifer-II is assumed to be t_p=2,000 h and t_p=300 h, respectively. Note that for $t > t_p$, only water (without viruses) was entering the aquifer.

The migration of bacteriophage MS2 in Aquifer-I and Aquifer-II was simulated with the transport model described by equations (1–10), using the physical and model parameters listed in Table 1. The mean collision efficiency was set to μ_α=0.0048 (Syngouna & Chrysikopoulos, 2011), in both aquifers. However, for Aquifer-I four different standard deviations of the collision efficiency were considered: (i) σ_α=0.0 (CV = 0%, geochemically homogeneous aquifer, spatially invariant α); (ii) σ_α=0.0024 (CV = 50%) (Flynn et al., 2004); (iii) σ_α=0.0048 (CV = 100%); and (iv) σ_α=0.0082 (CV = 170%). Whereas, for Aquifer-II two different standard deviations of the collision efficiency were considered: (i) σ_α=0.0 (CV = 0%); and (ii) σ_α=0.0082 (CV = 170%). All simulations conducted in this study represent ensemble averages of several model runs based on different random realizations of the spatially variable collision efficiency, generated by the exponential

(a)

(b)
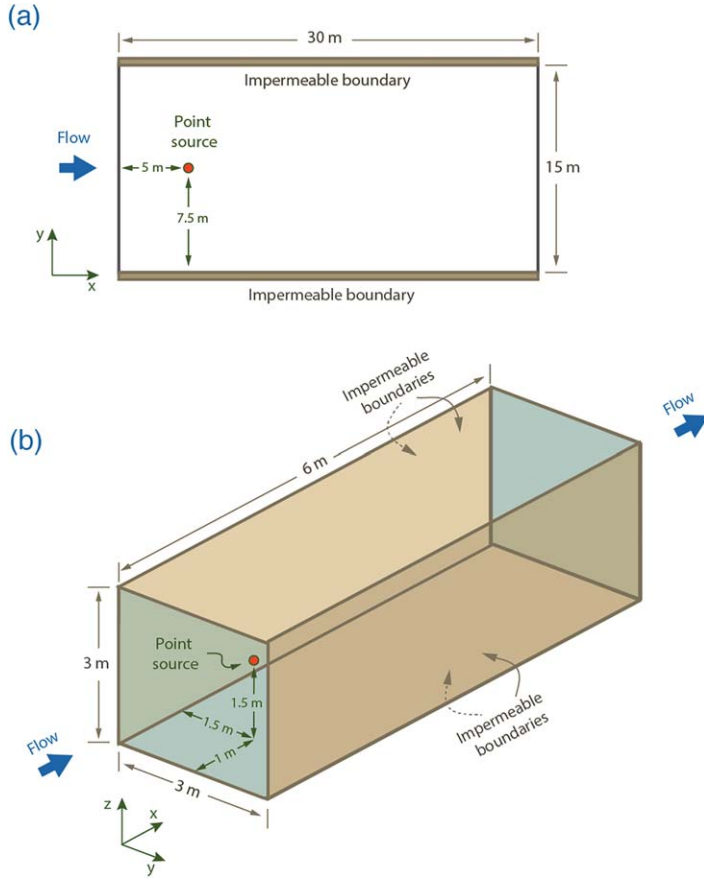
Figure 3. Schematic illustrations of the two aquifers considered in this study: (a) Aquifer-I, a two-dimensional aquifer with length $L_x=30$ m and width $L_y=15$ m, (b) Aquifer-II, three-dimensional aquifer with length $L_x=6$ m, width $L_y=3$ m and thickness $L_z=3$ m. The impermeable boundaries, flow direction, as well as the location of the point source are shown.

covariance function (25) or (27), for reversible ($r_{b*-b} \neq 0$) or irreversible ($r_{b*-b}=0$) attachment. Additionally, the two different source time periods employed ($t_p=300$ and 2,000 h) were carefully selected to ensure that over the simulation time period, negligible biocolloid mass migrated beyond the specified aquifer boundaries, so that the spatial moments defined by equations (30) and (31) were not violated and the results were meaningful.

The required number of model runs was determined by satisfying the following two criteria: (i) setting the maximum relative change of the 100-point rolling sample mean of the first normalized spatial moment in the longitudinal direction, $(\mu_M)_q=\langle M^s_{100}\rangle_q$, equal to 5×10^{-4}, where $q=100$ is the rolling sample, and (ii) prespecifying the acceptable uncertainty associated with the calculation of the ensemble mean, $\mu_M=\langle M^s_{100}\rangle$, given the sample mean, $(\mu_M)_q=(1/q)\sum_{i=1,q}(M^s_{100})_i$, and sample variance, $(\sigma^2_M)_q=1/(q-1)\sum_{i=1,q}[(M^s_{100})_i-(\mu_M)_q]^2$. Note that the sample mean is not expected to coincide with the ensemble mean, $(\mu_M)_q \neq \mu_M$, and the sample variance is not expected to coincide with the ensemble variance, $(\sigma^2_M)_q \neq \sigma^2_M$, of the random process. However, assuming that M^s_{100} follows an unknown distribution, then the Chebyshev inequality can be used to calculate the upper bounds of the confidence intervals related to the ensemble mean μ_M (Papoulis, 2002). Recall that the Chebyshev inequality states that the probability that a randomly selected value from an unknown (generic) distribution lies in the interval $\mu \pm k \cdot \sigma$ is at least $1-1/k^2$ (where μ and σ is the mean and standard deviation of the unknown distribution, and k is a positive real number). Applying the Chebyshev inequality to calculate the confidence intervals of the ensemble mean μ_M and using $(\sigma_M)_q/\sqrt{q}$ as an estimator of $\sigma_M/\sqrt{q}$, yields the following expression (Ballio & Guadagnini, 2004; Montgomery & Runger, 2013):

$$\Pr[(\mu_M)_q-k\frac{(\sigma_M)_q}{\sqrt{q}} \leq \mu_M \leq (\mu_M)_q+k\frac{(\sigma_M)_n}{\sqrt{q}}] \geq 1-\frac{1}{k^2} \quad (39)$$

where $1-1/k^2$ is the probability that the ensemble mean, μ_M, lies within the confidence interval around the sample mean $(\mu_M)_q$. In this work, the criterion (ii) was satisfied by predefining the 90% confidence interval ($k=3.16$; $1-1/k^2=0.9$), and by prespecifying the following upper bound for the ratio:

$$k\frac{(\sigma_M)_q}{\sqrt{q}(\mu_M)_q} < 1\times10^{-2} \quad (40)$$

Clearly, the uncertainty associated with the prediction of μ_M reduces as the sample size q increases. Worthy to note is that the Chebyshev inequality can be applied to unknown distributions, but may overestimate confidence intervals and produce conservative (safe) results.

The behavior of $\langle M^s_{100}\rangle_q$ as a function of the number of realizations of the spatially variable α, under reversible attachment, is illustrated in Figures 4a and 4b for Aquifer-I and in Figure 4c for Aquifer-II. Note that the required number of realizations increases with increasing variability of α, and it is larger for Aquifer-II (three-dimensional) than Aquifer-I (two-dimensional).

6. Discussion

6.1. Virus Transport Simulations
Contour snapshots on the x–y plane, of bacteriophage MS2 concentrations in isotropic Aquifer-I ($t_p=13 \times 10^3$ h) at various times, for the cases of geochemical homogeneity (CV = 0%) and heterogeneity

Table 1
Physical and Model Parameters

Parameter	Value (units)	Reference
U_x	2 (cm/hr)	Chrysikopoulos et al. (2012)
$\mu_{r_{b-b*}}$	0.119 (1/hr)	Equation (12)
$\mu_{r_{b*-b}}$	0.03 (1/hr)	Vasiliadou and Chrysikopoulos (2011)
λ_b	0 (1/hr)	Syngouna and Chrysikopoulos (2011)
λ_b^*	0 (1/hr)	Syngouna and Chrysikopoulos (2011)
θ	0.42 (–)	Syngouna and Chrysikopoulos (2011)
ζ_α	$0.2 \times L_x$ (cm)	–
t_p	300, 2,000, 8,000, 13,000 (hr)	–
A_{123}	9.72×10^{-10} (kg cm^2/h^2)	Murray and Parks (1980)
k_B	1.78×10^{-12} (kg cm^2/(hr^{2}K))	-
d_b	2.5×10^{-6} (cm)	Chrysikopoulos and Syngouna (2012)
d_c	0.06 (cm)	
ρ_b	1.42×10^{-3} (kg/cm^3)	Walshe et al. (2010)
ρ_s	1.61×10^{-3} (kg/cm^3)	
ρ_w	9.997×10^{-4} (kg/cm^3)	
μ_w	3.2×10^{-2} (kg/(cm hr))	
T	298 (K)	
μ_α	0.0048 (–)	Syngouna and Chrysikopoulos (2011)
CV	50 (%)	Flynn et al. (2004)
g	1.271×10^{10} (cm/hr^2)	
Two dimensional Transport		
D_x	30 (cm^2/h)	
D_y	12 (cm^2/h)	
D_z		
$L_x \times L_y$	30 (m) $\times$ 15 (m)	
n_x, n_y	401, 131	
Δt	3.5 (hr)	
Three dimensional Transport		
D_x	20 (cm^2/h)	
D_y	6 (cm^2/h)	
D_z	6 (cm^2/h)	
$L_x \times L_y \times L_z$	6 (m) $\times$ 3 (m) $\times$ 3 (m)	
n_x, n_y, n_z	101, 31, 31	
Δt	2.5 (hr)	

(CV = 170%) are presented in Figure 5. The contours in Figures 5a–5g are based on CV = 0%, and those in Figures 5h–5n are based on CV = 170%. Furthermore, the contours in Figures 5a–5n account for reversible attachment with average attachment rate coefficient $\mu_{r_{b-b*}}$ =0.119 1/hr and average detachment rate coefficient $\mu_{r_{b*-b}}$ =0.03 1/hr; whereas, the contours in Figures 5o–5u) account for irreversible attachment with $\mu_{r_{b-b*}}$ =0.005 1/hr and $\mu_{r_{b*-b}}$ =0 1/hr. It should be noted that the contours in Figures 5h–5u were based on the same random realization of the spatially variable α. Furthermore, the contour snapshots in Figures 5h–5n were constructed with μ_α=0.0048 and those in Figures 5o–5u with μ_α=0.0002. The selected μ_α value is considerably greater for reversible than irreversible attachment, because reversible and irreversible attachment can be considered to represent deposition in secondary minimum ("fast" deposition) and primary minimum ("slow" deposition), respectively (Tufenkji & Elimelech, 2005). Clearly, for the case of reversible attachment at late times, the virus plume for the geochemically heterogeneous case (see Figure 5l) is practically identical to the corresponding one for the geochemically homogeneous case (see Figure 5e). At late times, the migrating virus plume has sampled all possible geochemical variabilities within the isotropic, two-dimensional aquifer and the system has reached an "apparent equilibrium." Therefore, for the case of reversible attachment, at late times, virus transport was no longer affected by the spatial variability of α, because the rate of virus mass attachment and detachment at each spatial location within the aquifer became equal (local equilibrium). Consequently, at late times, Aquifer-I with reversible attachment behaved as an effective geochemical homogeneous aquifer. For the case of irreversible attachment, at late times, the system also reached an apparent equilibrium (see Figures 5q–5s). However, the virus plume was not symmetric (see Figure 5s), its shape was substantially different than the one obtained for the geochemically
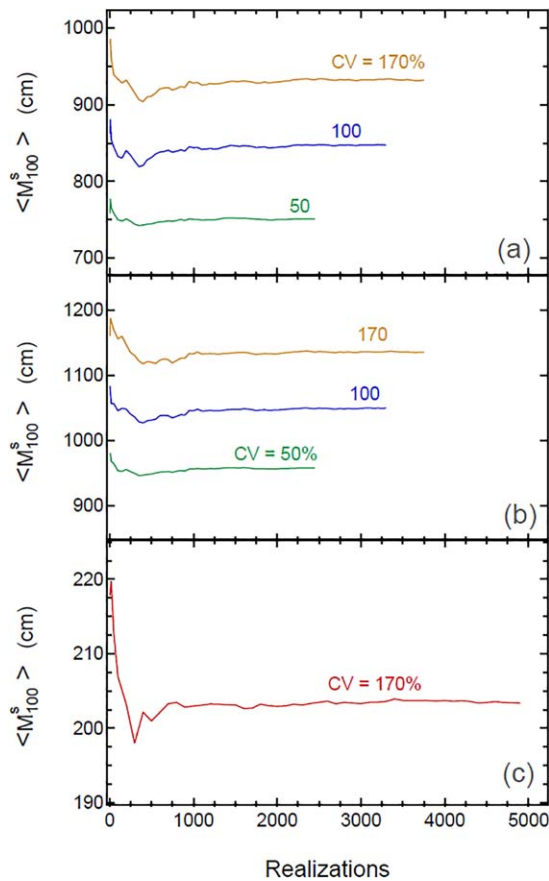
Figure 4. Ensemble mean of the first normalized spatial moment $\langle M_{100}^s \rangle$ in the longitudinal direction of the virus concentration distribution as a function of the number of random realizations of the spatially variable collision efficiency, assuming reversible attachment in: (a) in the geochemical isotropic Aquifer-I at $t = 1 \times 10^3$ h, (b) in the geochemical isotropic Aquifer-I at $t = 2 \times 10^3$ h, and (c) in the geochemical anisotropic Aquifer-II at $t = 300$ h.

homogeneous case (see Figure 5e). Note that for the case of irreversible attachment, two adjacent locations within the heterogeneous aquifer may have similar suspended virus concentrations but considerably different attachment rate coefficients, resulting in nonsymmetric suspended virus concentration plumes. The contours in Figures 5f, 5g, 5m, 5n, 5t, and 5u (last two rows in Figure 5) were constructed for times greater than the source release time period ($t > t_p = 1,30,00$ h) and clearly show that geochemical heterogeneity led to retarded migration (delayed exit) of the suspended virus concentration. Suspended viruses remained over greater areas within the geochemically heterogeneous (see Figures 5m and 5n) than the geochemically homogeneous aquifers (see Figures 5f and 5g); whereas, for the case of irreversible attachment, the suspended virus concentrations progressively disappeared (see Figures 5t and 5u). This retarded biocolloid migration, which is caused by increased spreading in both upstream and downstream directions, is not intuitive; however, it is similar to the results observed in previous studies of contaminant transport with spatially variable retardation (Chrysikopoulos et al., 1990a, 1992a, 1992b).

A three-dimensional iso-volume representation of a single random realization of the spatially variable collision efficiency for an isotropic Aquifer-II ($\zeta_\alpha = 1.2$ m, $t_p = 8 \times 10^3$ h) is illustrated in Figure 6a. The corresponding three-dimensional iso-volume representations of suspended virus concentration, C_b, and virus concentration attached onto the solid matrix, C_b^*, at $t = 1 \times 10^4$ h under reversible attachment, are illustrated in Figures 6b and 6c, respectively. Figure 6d illustrates the three-dimensional iso-volume representation shown in Figure 6a, but sliced at $y = 180$ cm. Three-dimensional iso-surface representations of C_b and C_b^*, sliced at $y = 180$ cm are illustrated in Figures 6e and 6f, respectively. The center of mass in Figures 6b, 6c, 6e, and 6f has moved downstream, because the simulation time was greater than the source time period, t_p. Consequently, virus concentration previously attached in the upstream portion of Aquifer-II has been detached and migrated downstream. It is noteworthy that there is an obvious correlation between the intensity of α and the magnitude of both C_b and C_b^* (compare Figure 6d with Figures 6e and 6f). The iso-volumes presented in Figures 6b and 6c exhibit volume similarities, and the iso-surfaces presented in Figure 6e and 6f exhibited strength similarities. These similarities were controlled by the distribution of α within the three-dimensional Aquifer-II.

The iso-volume and iso-surface representations of virus concentration in isotropic Aquifer-II ($\zeta_\alpha = 1.2$ m, $t_p = 8 \times 10^3$ h) at $t = 400$, 2.000, and 5,000 h are presented in Figure 7. The case of isotropic geochemical heterogeneity (CV = 170%) with reversible attachment ($\mu_{r_{b-b*}} = 0.119$ 1/hr, $\mu_{r_{b*-b}} = 0.03$ 1/hr), is shown in Figures 7c–7h,o-t, whereas case of isotropic geochemical heterogeneity (CV = 170%) with irreversible attachment ($\mu_{r_{b-b*}} = 0.005$ 1/hr and $\mu_{r_{b*-b}} = 0$ 1/hr) is shown in Figures 7i–7n and 7u–7z. For the case of reversible attachment at late times ($t = 5,000$ h), the virus concentration plume for the geochemically heterogeneous case (see Figures 7e and 7h) was symmetrical, despite earlier ($t = 2,000$ h) deviation from symmetry (see Figures 7d and 7g). In contrast, for the case of irreversible attachment the virus concentration plume remained non-symmetric (see Figures 7k and 7n). This was attributed to the fact that under reversible attachment, at late times, the migrating virus plume already sampled all possible geochemical variabilities within the Aquifer II and reached a uniform apparent equilibrium, while this was not possible for irreversible attachment. Note that the virus mass attached onto the solid matrix at early times ($t = 400$ h) for reversible attachment exhibited higher concentration values near the source location ($x_0 = 100$ cm, $y_0 = 150$ cm, $z_0 = 150$ cm) than for irreversible attachment (see Figures 7r and 7x). However, at late times ($t = 5,000$ h) this behavior was reversed (see Figures 7t and 7z). This shift in virus mass was attributed to the different
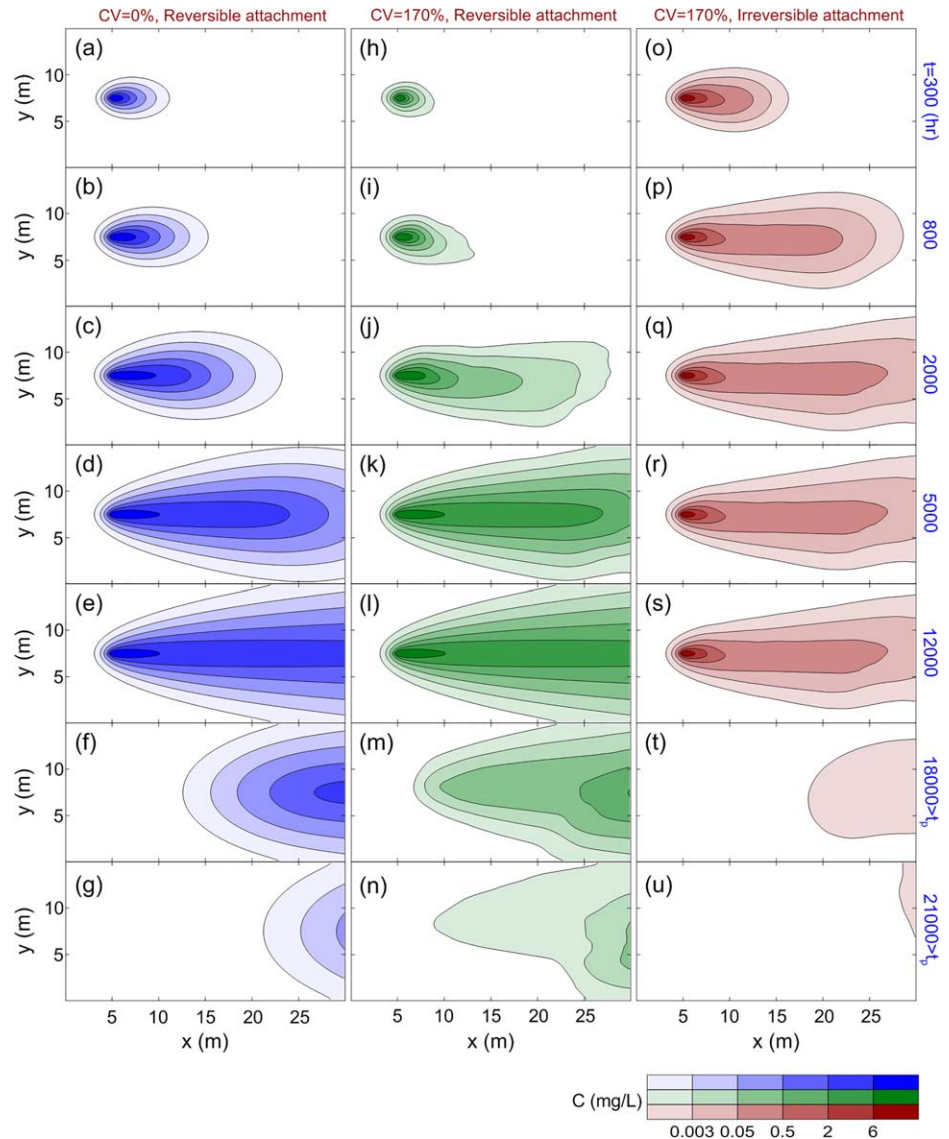
Figure 5. Contour plots on the x–y plane for suspended virus concentration in Aquifer-I at seven different times (t = 300, 800, 2,000, 5,000, 12,000, 18,000 and 21,000 h), accounting for: (a-g) geochemical homogeneity (CV = 0%) with reversible attachment ($r_{b-b*} \neq 0$, $r_{b*-b} \neq 0$), (h-n) isotropic geochemical heterogeneity (CV = 170%) with reversible attachment ($r_{b-b*} \neq 0$, $r_{b*-b} \neq 0$), and (o-u) isotropic geochemical heterogeneity (CV = 170%) with irreversible attachment ($r_{b-b*} \neq 0$, $r_{b*-b} = 0$). Here, $t_p = 13{,}000$ h, $\mu_{r_{b-b*}} = 0.119$ 1/hr, and $\mu_{r_{b*-b}} = 0.03$ 1/hr.

$\mu_{r_{b-b*}}$ and $\mu_{r_{b*-b}}$ values used for the simulations. Because $\mu_{r_{b-b*}}$ was greater for reversible (0.119 1/hr) than irreversible (0.005 1/hr) attachment, at early times the attached virus mass was greater for the case of reversible attachment. At late times, the total virus mass attached was greater for the case of irreversible than reversible attachment.

6.2. Moment Analysis

The effect of spatially variable attachment on biocolloid transport in Aquifer-I and Aquifer-II was investigated by traditional moment analysis. The ensemble mean of the zeroth absolute spatial moment, $\langle m^s_{000} \rangle$, and the ensemble mean of the first normalized spatial moment in the longitudinal direction, $\langle M^s_{100} \rangle$, were calculated for the suspended biocolloids in the geochemically heterogeneous aquifers with spatially variable collision efficiency. Furthermore, the ensemble mean of the zeroth absolute spatial moment, $\langle m^s_{000}(C*) \rangle$, for the biocolloids attached onto the solid matrix in the geochemically heterogeneous aquifers
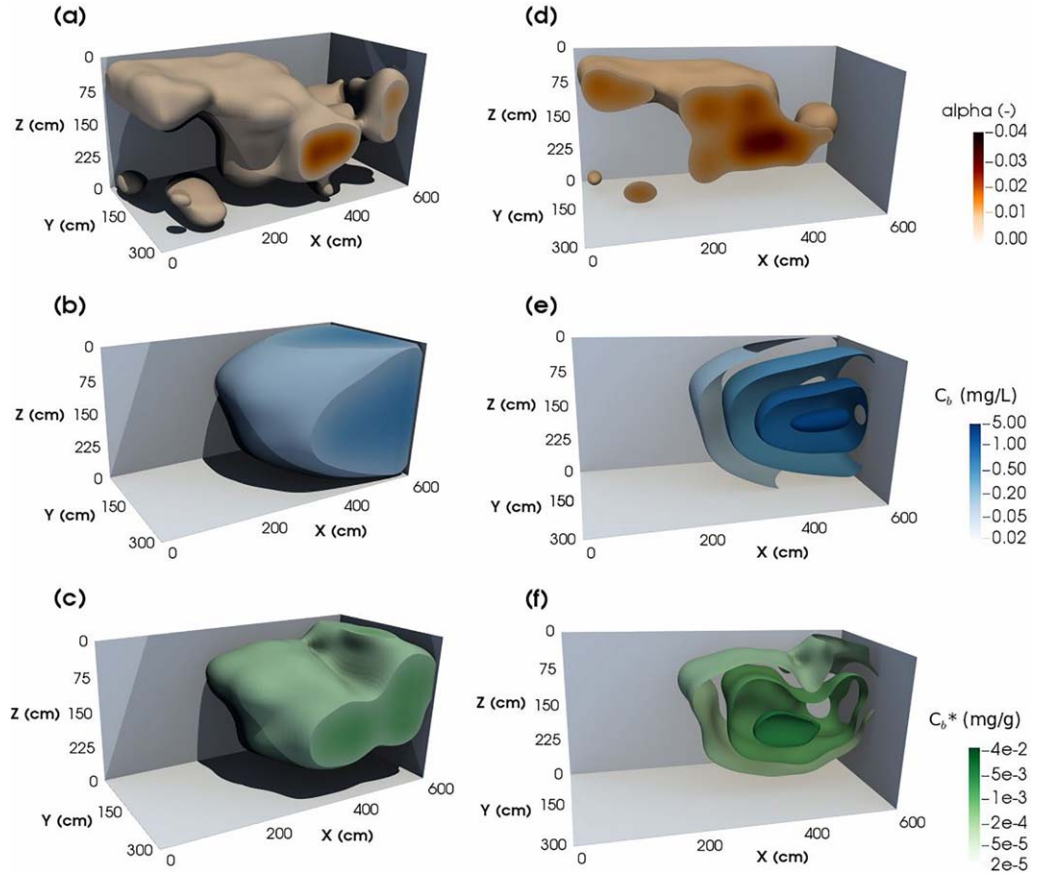
Figure 6. For the isotropic Aquifer-II (ζ_α=1.2 m), iso-volume representations for: (a) a single random realization of the spatially variable collision efficiency, (b) suspended virus concentration, (c) virus concentration attached onto the solid matrix, and (d) the realization shown in (a) sliced at y = 180 cm. Also, iso-surface representations sliced at y = 180 cm for: (e) suspended virus concentration, and (f) virus concentration attached onto the solid matrix. Here, $\mu_{r_{b-b*}}$ =0.119 1/hr, $\mu_{r_{b*-b}}$ =0.03 1/hr, CV=σ_α/μ_α=170%, t = 1 × 10⁴ h and t$_p$=8 × 10³ h.

with spatially variable collision efficiency was determined from equation (30) by replacing C_b with C_b^*. Additionally, for convenience, the following moment ratios were introduced:

$$mR = \frac{\langle m_{000}^s \rangle}{m_{000}^{s-(h)}} \tag{41}$$

$$mR(C_*) = \frac{\langle m_{000}^s(C_*) \rangle}{m_{000}^{s-(h)}(C_*)} \tag{42}$$

$$MR = \frac{\langle M_{100}^s \rangle}{M_{100}^{s-(h)}} \tag{43}$$

where the exponent "(h)" was used in $m_{000}^{s-(h)}$, $m_{000}^{s-(h)}(C_*)$ and $M_{100}^{s-(h)}$ to denote that the moments were evaluated for the case of spatially invariant collision efficiency (geochemically homogeneous aquifer). For $mR > 1$ and $mR(C_*) > 1$ there is more biocolloid mass suspended and attached, respectively, in the geochemically heterogeneous than the geochemically homogeneous aquifer. Also, for $MR > 1$ the migration of the center of the suspended biocolloid mass in the geochemically heterogeneous aquifer is accelerated compared to the geochemically homogeneous aquifer.

The following ratios of the spatial covariance, S_{ii}^2 (where the subscripts "ii = xx,yy,zz" represent direction), of the second normalized spatial moments about the center of mass, as defined in equation (33), were also introduced:
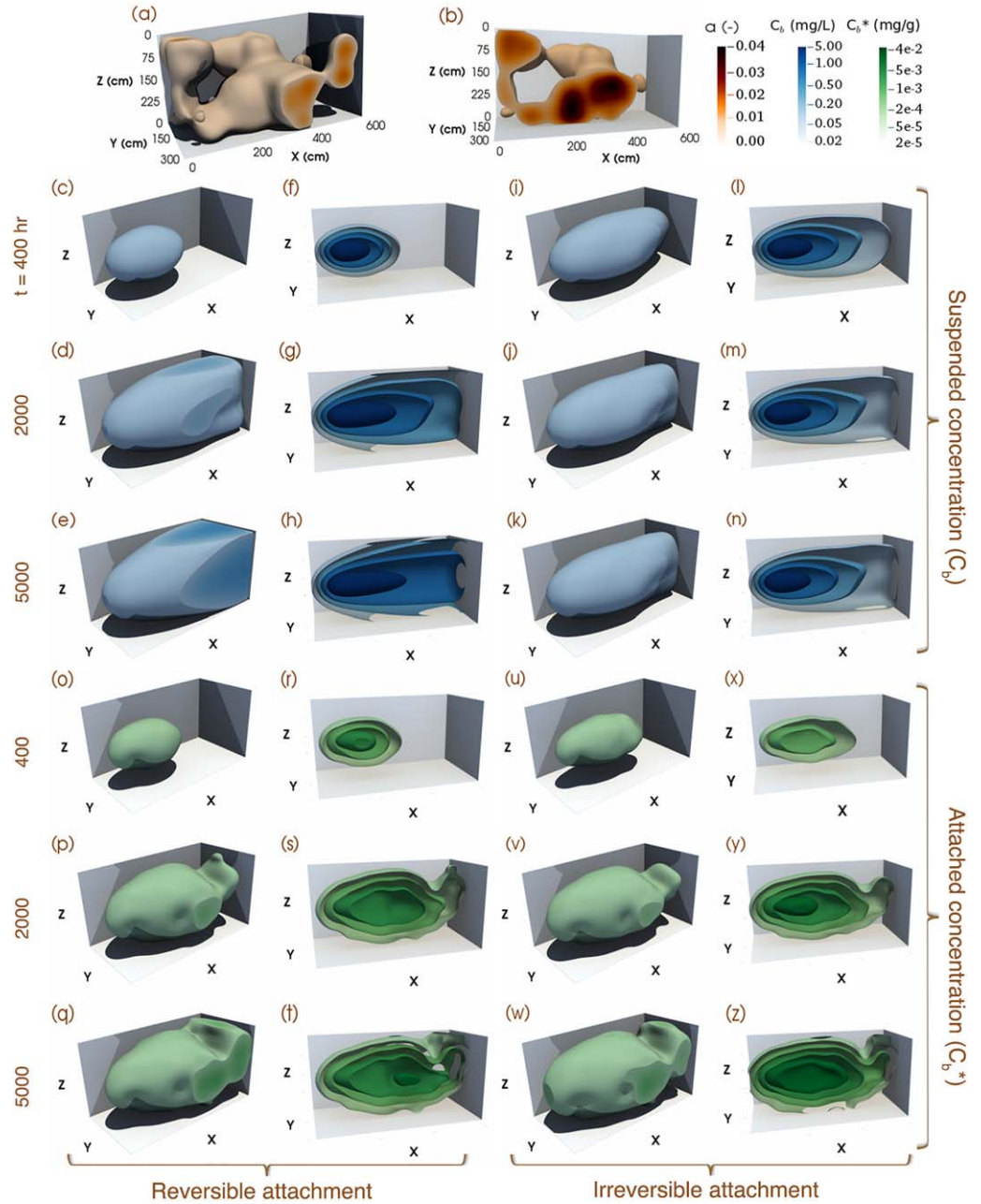
Figure 7. Iso-volume and iso-surface representations of virus concentration in isotropic Aquifer-II, at three different times for: (a,b) a single random realization of the spatially variable collision efficiency, (c-h, o-t) isotropic geochemical heterogeneity (CV=σ_α/μ_α=170%) with reversible attachment ($r_{b-b*}\neq0$, $r_{b*-b}\neq0$), and (i-n, u-z) isotropic geochemical heterogeneity (CV = 170%) with irreversible attachment ($r_{b-b*}\neq0$, $r_{b*-b}=0$). The realization shown in (a) was also presented in (b) sliced at y = 180 cm. The iso-surface representations of suspended virus concentration (c-e, i-k) were also presented in (f-h, l-n) sliced at y = 180 cm. The representations of virus concentration attached onto the solid matrix shown in (o-q, u-w) were also presented in (r-t, x-z) sliced at y = 180 cm. Reversible attachment is shown in the left two columns and irreversible attachment in the right two columns. Here, ζ_α=1.2 m, t_p=8 × 10^3 h.

$$S_{ii}^2 R = \frac{\langle S_{ii}^2 \rangle}{S_{ii}^{2-(h)}} \tag{44}$$

where the angle brackets "$\langle\rangle$" represent ensemble mean, and exponent "(h)" in $S_{ii}^{2-(h)}$ was used to denote that the spatial covariance was evaluated for the case of spatially invariant collision efficiency (geochemically
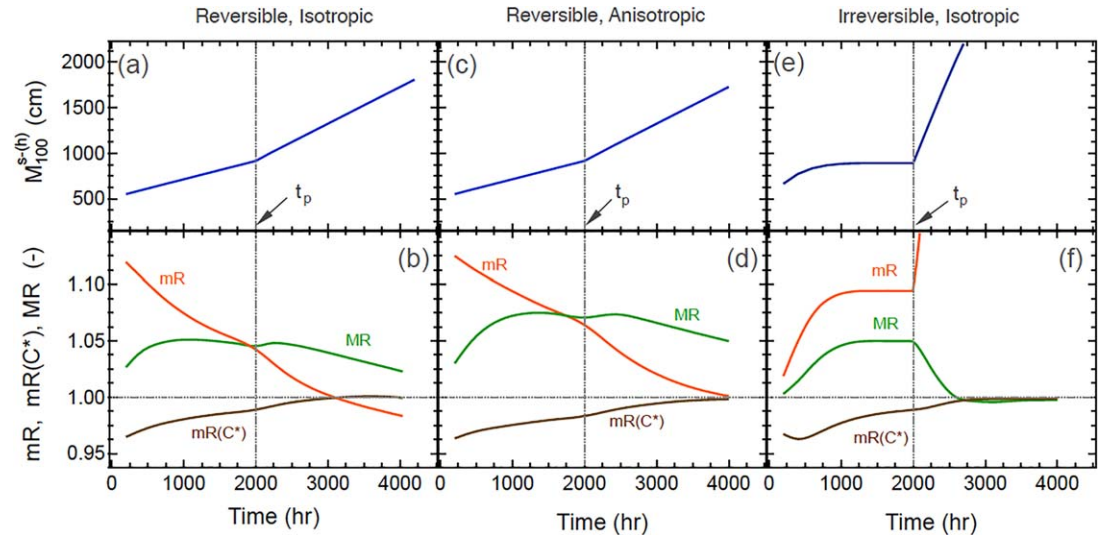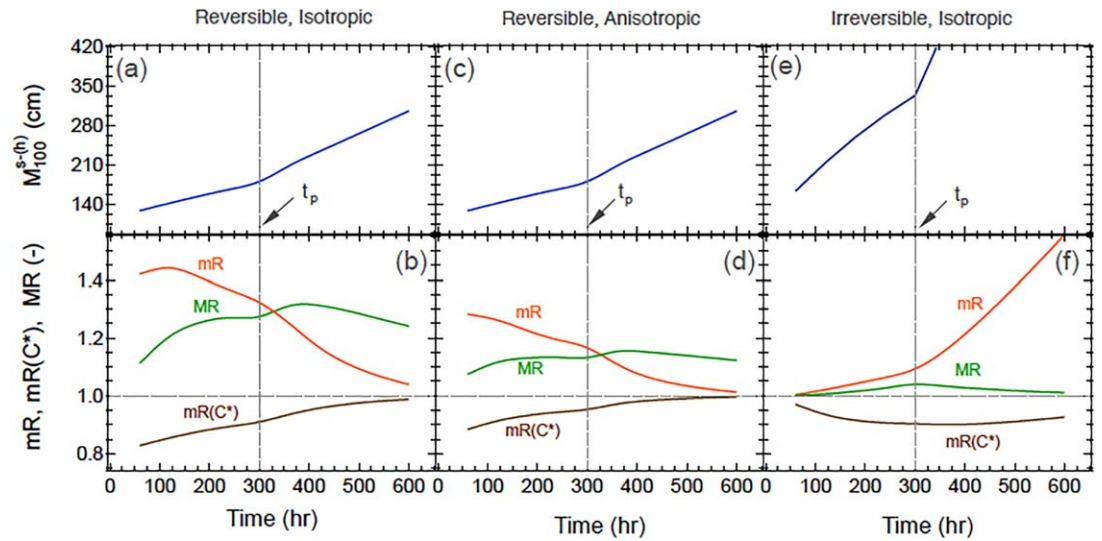
Figure 8. Time history of the first normalized spatial moment in the longitudinal direction of bacteriophage MS2, $M_{100}^{s-(h)}$, and for the ratios mR, mR(C*), and MR in the two-dimensional Aquifer-I under both geochemically homogeneous and heterogeneous conditions, assuming: (a,b) reversible attachment and isotropic ($\zeta_\alpha = 6$ m) geochemical heterogeneity, (c,d) reversible attachment and anisotropic ($\zeta_{\alpha x} = 15$ m, $\zeta_{\alpha y} = 6$ m) geochemical heterogeneity, and (e,f) irreversible attachment and isotropic ($\zeta_\alpha = 6$ m) geochemical heterogeneity. Here, $t_p = 2 \times 10^3$ h, $CV = \sigma_\alpha / \mu_\alpha = 0\%$ for geochemical homogeneity, and CV = 50% for geochemical heterogeneity.

homogeneous aquifer). Spatial covariance ratios greater than one, $S_{ii}^2 R > 1$, indicate that the spreading about the center of the mass is greater in a geochemically heterogeneous (isotropic or anisotropic) than geochemically homogeneous aquifer. The opposite is true for $S_{ii}^2 R < 1$. Also, the ratios of the hydrodynamic dispersion coefficient, D_{ii} (where the subscripts "ii = xx,yy,zz" represent direction), were introduced:

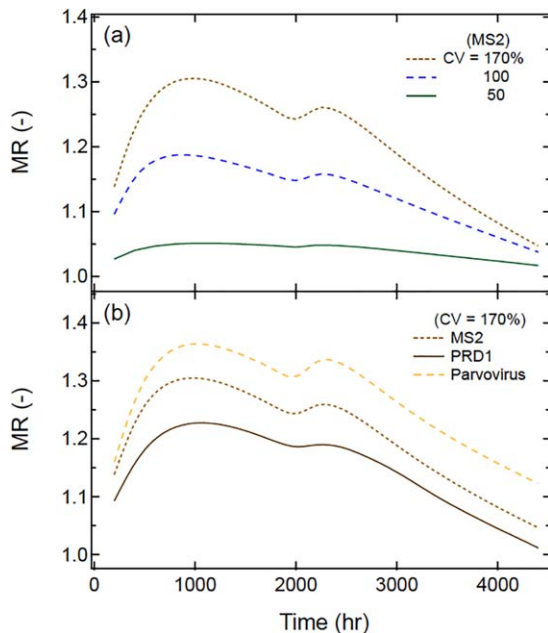$$D_{ii}R = \frac{\langle D_{ii} \rangle}{D_{ii}^{(h)}} \qquad (45)$$

The transport behavior of bacteriophage MS2 in the two-dimensional Aquifer-I for both cases of geochemical homogeneity (CV = 0%), and heterogeneity (CV = 50%, $t_p = 2 \times 10^3$ h) is illustrated in Figure 8, over a time period of 4,000 h. The first normalized spatial moment in the longitudinal direction, $M_{100}^{s-(h)}$, as well as the ratios $mR = \langle m_{000}^s \rangle / m_{000}^{s-(h)}$, $mR(C*) = \langle m_{000}^s(C*) \rangle / m_{000}^{s-(h)}(C*)$, and $MR = \langle M_{100}^s \rangle / M_{100}^{s-(h)}$ were determined for the cases of reversible attachment with isotropic ($\zeta_\alpha = 6$ m) geochemical heterogeneity (see Figures 8a and 8b), reversible attachment with anisotropic ($\zeta_{\alpha x} = 15$ m, $\zeta_{\alpha y} = 6$ m) geochemical heterogeneity (see Figures 8c and 8d), and irreversible attachment with isotropic ($\zeta_\alpha = 6$ m) geochemical heterogeneity (see Figures 8e and 8f). For the cases of reversible attachment under both isotropic and anisotropic geochemical heterogeneity, the $M_{100}^{s-(h)}$ time histories, as calculated with equation (31), were shown to monotonically increase with time and to exhibit a change in slope after the end of the source release time period $t = t_p = 2,000$ h (see Figures 8a and 8c). However, for irreversible attachment with isotropic geochemical heterogeneity, the values of $M_{100}^{s-(h)}$ were shown to progressively increase, then remain constant till $t = t_p = 2,000$ h, and subsequently increased again (see Figure 8e). Clearly, for the two cases of reversible attachment considered here, the migrating virus plume did not have enough time to reach a steady-state over the time period t_p (note that the center of the mass in Figures 8a and 8c continuously migrated downstream), whereas for the irreversible attachment the migrating virus plume reached a steady-state over the time period $1,000$ h $< t < t_p$ (note that the center of the mass in Figure 8e was not moving downstream during steady-state). At steady-state $M_{100}^{s-(h)}$ remains stationary simply because the rate at which mass enters the aquifer from the source equals the rate at which mass is attached onto the solid matrix of the aquifer. This steady-state behavior can also be observed in Figures 5q, 5r, and 5s (where $t_p = 13,000$ h).

The values of MR for both isotropic and anisotropic cases under reversible attachment (see Figures 8b and 8d) progressively increased during the time interval from $t = 200$ to $1,000$ h, as the virus plume expanded in the aquifer and encountered unsampled regions of heterogeneity. Over the time period $t = 1,000$ to
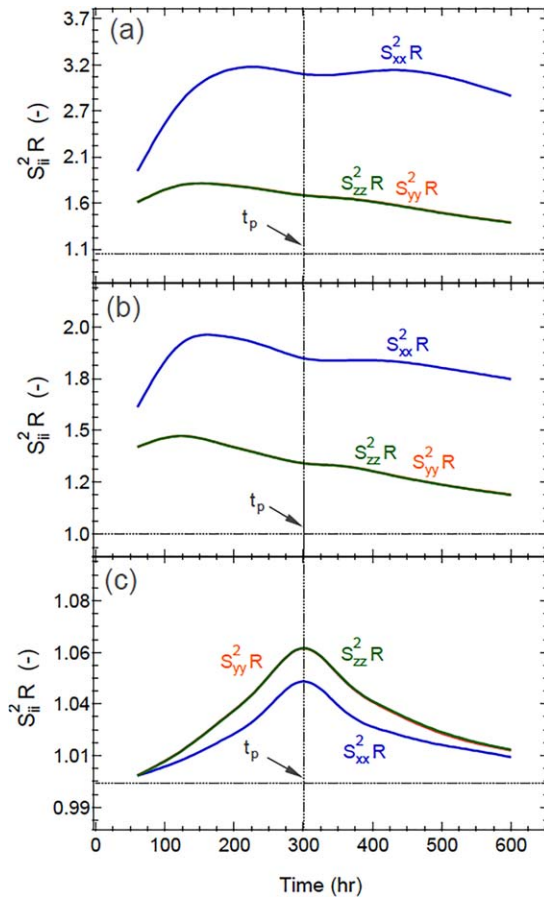
Figure 9. Time history of the first normalized spatial moment in the longitudinal direction of bacteriophage MS2, $M_{100}^{s-(h)}$, and for the ratios mR, mR(C*), and MR in the three-dimensional Aquifer-II under both geochemically homogeneous and heterogeneous conditions, assuming: (a,b) reversible attachment and isotropic (ζ_α=1.2 m) geochemical heterogeneity, (c,d) reversible attachment and anisotropic ($\zeta_{\alpha x}$=0.24 m, $\zeta_{\alpha y}$=1.2 m, $\zeta_{\alpha z}$=1.2 m) geochemical heterogeneity, and (e,f) irreversible attachment and isotropic geochemical heterogeneity (ζ_α=1.2 m). Here, t_p=300 h, $CV = \sigma_\alpha/\mu_\alpha$=0% for geochemical homogeneity, and CV = 170% for geochemical heterogeneity.

2,000 h the unsampled regions within the aquifer decreased, which in turn yielded a slight decrease in the MR values. After the end of the source release time period (t = t_p=2,000 h) the MR values increased slightly and then eventually started to decrease again as the system progressively sampled most of the aquifer geochemical heterogeneity. Also, the time histories of mR and mR(C*) ratios under reversible attachment were illustrated in Figures 8b and 8d. Note that mR values decreased monotonically, with values greater than unity at early times. Furthermore, values mR < 1 in Figure 8b occurred only temporarily, because the biocolloid plume in the non-homogeneous case has moved further downstream due to the increased spreading (MR > 1) where the aquifer was free of attached biocolloids. At larger times, mR is expected to asymptotically reach unity. Clearly, the effects of the spatially variable α fade with time, as the virus plume sampled all of the aquifer geochemical heterogeneity. The mR(C*) values increased monotonically, with values lower than unity at early times and values close to unity at late times, indicating that at late times the total attached virus mass was equal for both homogeneous and heterogeneous aquifers. However, for the case of irreversible attachment with isotropic geochemical heterogeneity, the time histories of mR, mR(C*) and MR (Figures 8e and 8f) were substantially different than those obtained for the case of reversible attachment (Figures 8a–8d). At early times, mR and MR were shown to progressively increase, maintaining values greater than unity, then remained constant till t = t_p=2,000 h, and subsequently mR increased sharply (in a fashion similar to $M_{100}^{s-(h)}$ in Figure 8e), while MR decreased sharply. Clearly, at early times, the spatial variability of α enhanced the spreading of suspended viruses. At late times (in the absence of the virus source), for the case of irreversible attachment, the value of MR ratio was shown to fluctuate and approach unity (see Figure 8f), because most of the virus mass was already attached onto the solid matrix of Aquifer-I. Finally, the mR(C*) time history for irreversible attachment (see Figure 8f), exhibited small

Figure 10. Behavior of the ratio MR as a function of time in isotropic Aquifer-I for: (a) MS2 migration with three different coefficients of variation, and (b) migration of three different viruses with $CV = \sigma_\alpha/\mu_\alpha$=170%. Here, t_p=2 × 10³ h.

Figure 11. Time history of $S_{ii}^2 R$ for the migration of MS2 in Aquifer-II, assuming: (a) reversible attachment and isotropic geochemical heterogeneity, (b) reversible attachment and anisotropic geochemical heterogeneity, and (c) irreversible attachment and isotropic geochemical heterogeneity. Here, t_p=300 h, $CV = \sigma_\alpha/\mu_\alpha$=0% for geochemical homogeneity, and CV = 170% for geochemical heterogeneity.

fluctuations at early times, then it was shown to increase monotonically, while maintaining values lower than unity. This behavior was expected because at late times, due to irreversible attachment, most of the virus mass was attached onto the solid matrix of both homogeneous and heterogeneous aquifers, and in turn mR(C*) approached unity.

The transport behavior of bacteriophage MS2 in the three-dimensional Aquifer-II for both cases of geochemical homogeneity (CV = 0%), and heterogeneity (CV = 170%) is illustrated in Figure 9 over a time period of 600 hours. The virus source release time period was set t_p=300 h. The first normalized spatial moment in the longitudinal direction, $M_{100}^{s-(h)}$, as well as the ratios mR, mR(C*) and MR were determined for reversible attachment and isotropic (ζ_α=1.2 m) geochemical heterogeneity (see Figures 9a and 9b); reversible attachment and anisotropic ($\zeta_{\alpha x}$=0.24 m, $\zeta_{\alpha y}$=1.2 m, $\zeta_{\alpha z}$=1.2 m) geochemical heterogeneity (see Figures 9c and 9d); and irreversible attachment and isotropic (ζ_α=1.2 m) geochemical heterogeneity (see Figures 9e and 9f). The resulting $M_{100}^{s-(h)}$, mR, mR(C*) and MR curves for the three-dimensional Aquifer-II (see Figure 9) followed similar trends as those obtained for the two-dimensional Aquifer-I (see Figure 8). The significant mR increase observed for t > t_p in Figures 8f and 9f is attributed to the very small amount of mass (∼2%) remaining in the liquid phase due to irreversible attachment, compared to the mass that has entered the aquifer from the source. Consequently, for t > t_p, small absolute differences in the mass of suspended colloids produce significant changes in mR ratios.

The behavior of the ratio MR=$\langle M_{100}^s \rangle / M_{100}^{s-(h)}$ for MS2 virus, as a function of time for three different values of the coefficient of variation (CV = 50, 100, and 170%) was illustrated in Figure 10a. For comparison, simulations were performed also for two additional viruses with different size (CV = 170%): PRD1 with diameter d = 62 nm and density ρ_b =1,348 kg/cm^3 (Olsen et al., 1974), and parvovirus with d = 18 nm, and ρ_b =1,420 kg/cm^3 (Bachmann et al., 1979). The corresponding average attachment rate coefficient evaluated from equations (11–23) is $\mu_{r_{b-b^*}}$ =0.058 and 0.160 1/hr for PRD1 and Parvovirus, respectively. The MR ratios for all three viruses (MS2, PRD1, Parvovirus) are illustrated in Figure 10b. The calculations were based on the assumption that virus attachment was reversible in the geochemically heterogeneous Aquifer-I (ζ_α=6 m) and t_p=2 × 10^3 h. Note that all six time history curves of MR exhibited values greater than unity (MR > 1) (see Figure 10). Also, the MR values were shown to increase with increasing CV or equivalently with increasing variability in α and decreasing particle diameter size (or increasing average attachment rate coefficient $\mu_{r_{b-b^*}}$). Clearly, the spatial variability of α enhanced the movement of the center of virus mass. These results are analogous to the enhanced migration and spreading of sorbing contaminants in porous media with spatially variable retardation (Chrysikopoulos et al., 1990a, 1992a, 1992b).

The behavior of the ratio of the second normalized spatial moments about the center of mass, $S_{ii}^2 R = \langle S_{ii}^2 \rangle / S_{ii}^{2-(h)}$ (where ii = xx,yy,zz), of a migrating bacteriophage MS2 (virus) plume in the three-dimensional anisotropic Aquifer-II as a function of time was illustrated in Figure 11. Three different cases were examined: (a) reversible attachment with isotropic (ζ_α=1.2 m) geochemical heterogeneity, (b) reversible attachment with anisotropic ($\zeta_{\alpha x}$=0.24 m, $\zeta_{\alpha y}$=1.2 m, $\zeta_{\alpha z}$=1.2 m) geochemical heterogeneity, and (c) irreversible attachment with isotropic (ζ_α=1.2 m) geochemical heterogeneity. Note that for all cases considered, $S_{xx}^2 R$, $S_{yy}^2 R$, and $S_{zz}^2 R$ were greater than unity throughout the duration of the simulations. Clearly, the spatial variability in α enhanced the spreading of the suspended virus plume. All $S_{ii}^2 R$ ratios at early times exhibited an increasing slope, reached a maximum value, and subsequently decreased (more rapidly at times t > t_p=300 h). For the first two cases of reversible attachment (CV = 170%) the
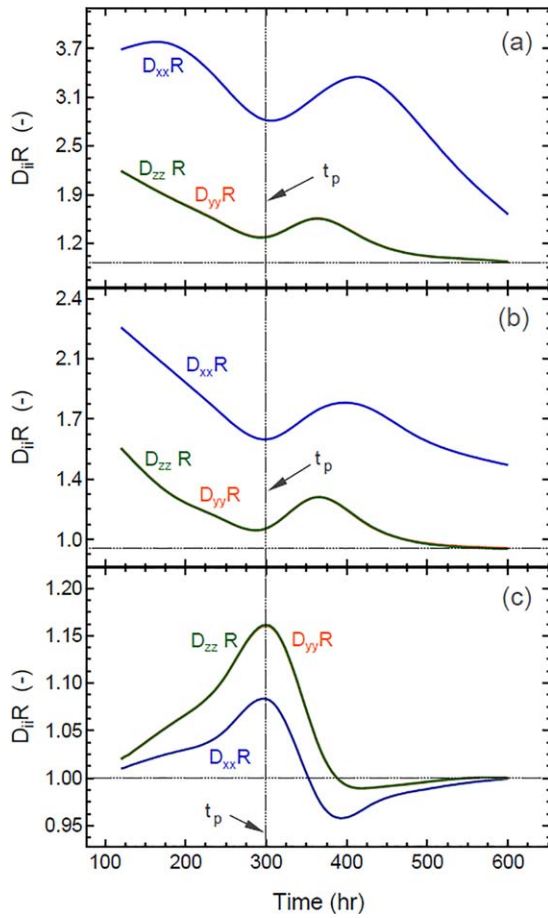
Figure 12. Time history of $D_{ii}R$ for the migration of MS2 in Aquifer-II, assuming: (a) reversible attachment and isotropic geochemical heterogeneity, (b) reversible attachment and anisotropic geochemical heterogeneity, and (c) irreversible attachment and isotropic geochemical heterogeneity. Here, $t_p = 300$ h, $CV = \sigma_\alpha/\mu_\alpha = 0\%$ for geochemical homogeneity, and $CV = 170\%$ for geochemical heterogeneity.

time histories of S_{ii}^2R in all three directions (xx,yy,zz) followed similar trends for both isotropic and anisotropic geochemical heterogeneity, and $S_{xx}^2R > S_{yy}^2R \simeq S_{zz}^2R$. However, for the third case of irreversible attachment with isotropic geochemical heterogeneity it was shown that $S_{xx}^2R < S_{yy}^2R \simeq S_{zz}^2R$.

The behavior of the ratio of the hydrodynamic dispersion coefficient, $D_{ii}R = \langle D_{ii} \rangle / D_{ii}^{(h)}$ (where ii = xx,yy,zz), of a migrating bacteriophage MS2 (virus) plume in the three-dimensional Aquifer-II as a function of time was illustrated in Figure 12 (for the exact same cases considered in Figure 11). Note that the time histories of $D_{ii}R$ followed similar patterns as the time histories of S_{ii}^2R, owing to the imposed relationship between D_{ii} and S_{ii}^2 (see Equation (34)). Therefore, the spatially variable α contributed to increased dispersion of the suspended virus plume. Note that only for the case of irreversible attachment the values of $D_{ii}R$ ratios are lower than unity over a small time period after t = 350 h (see Figure 12c). This unexpected result is attributed to the use of equation (34) for the calculation of $D_{ii}R$ ratios. Equation (34) was developed by Aris (1956) for a conservative tracer; thus, it is not fully applicable to cases of irreversibly attached viruses where the suspended virus mass is progressively reduced (see Figure 12c), although it is less problematic for reversibly attached viruses (see Figures 12a and 12b).

The effect of correlation length of the collision efficiency, α, on bacteriophage MS2 migration in the two-dimensional, geochemically heterogeneous Aquifer-I is illustrated in Figure 13. Anisotropic (variable $\zeta_{\alpha x}$, $\zeta_{\alpha y} = 6$ m, see Figures 13a–13c), as well as isotropic (variable $\zeta_\alpha = \zeta_{\alpha x} = \zeta_{\alpha y}$, see Figures 13d–13f) aquifers were considered. For the anisotropic aquifer case the ratios mR and MR exhibited an initial increase with increasing correlation length values and progressively reached a constant value or zero slope (see Figure 13a). On the contrary, the ratio mR(C*) exhibited an initial decrease before it reached a zero slope. This is an intuitive result because for mR > 1 more virus mass was found in the aqueous phase within the heterogeneous than the homogeneous Aquifer-I, which led to more virus mass attached onto the solid matrix in the homogeneous than in the heterogeneous Aquifer-I, and in turn led to mR(C*)<1. Similar behavior to mR and MR was observed for S_{ii}^2R (see Figure 13b) and $D_{ii}R$ (see Figure 13c). For the case of isotropic aquifer Aquifer-I, the ratios mR and MR exhibited an initial increase, reached a maximum value and progressively started to decrease again and to approach unity values (see Figure 13d). Whereas the mR(C*) exhibited an initial decrease before it approached unity (see Figure 13d). Also, similar behavior to mR and MR was observed for S_{ii}^2R (see Figure 13e) and $D_{ii}R$ (see Figure 13f). It is worthy to note that mR, MR, mR(C*), S_{ii}^2R and $D_{ii}R$ for anisotropic and isotropic cases exhibited very different behavior at large correlation lengths. The ratios approached unity only for the isotropic case because as $\zeta_\alpha \to \infty Z$ the correlation of the normally distributed collision efficiency in Aquifer-I became very low (effectively homogeneous, see covariance function (27)); however, this was not the case for the anisotropic case because as $\zeta_{\alpha x} \to \infty$ the value of $\zeta_{\alpha y}$ remained fixed (see covariance function (25)). Note that enhanced transport dissipated completely in the isotropic Aquifer-I ($S_{xx}^2R = S_{yy}^2R = D_{xx}R = D_{yy}R \cong 1.00$) for correlation length of $\zeta_\alpha > 3 \times 10^6$ m.

Figure 14 was constructed to show the vital importance of using the appropriate number of realizations of the spatially variable α for correct ensemble mean estimation. The time history of the MR ratio for the case of MS2 migration in the two-dimensional, geochemically heterogeneous and anisotropic ($\zeta_{\alpha x} = 15$ m, $\zeta_{\alpha y} = 6$ m) Aquifer-I was presented for five different realization numbers q (q = 80, 320, 1,280, 5,120, 10,000). The results for q = 5,120 and q = 10,000 are very similar, suggesting that there is convergence at large q. However, the curves for q = 80 and q = 320 have a substantially different shape. It is worthy to note that
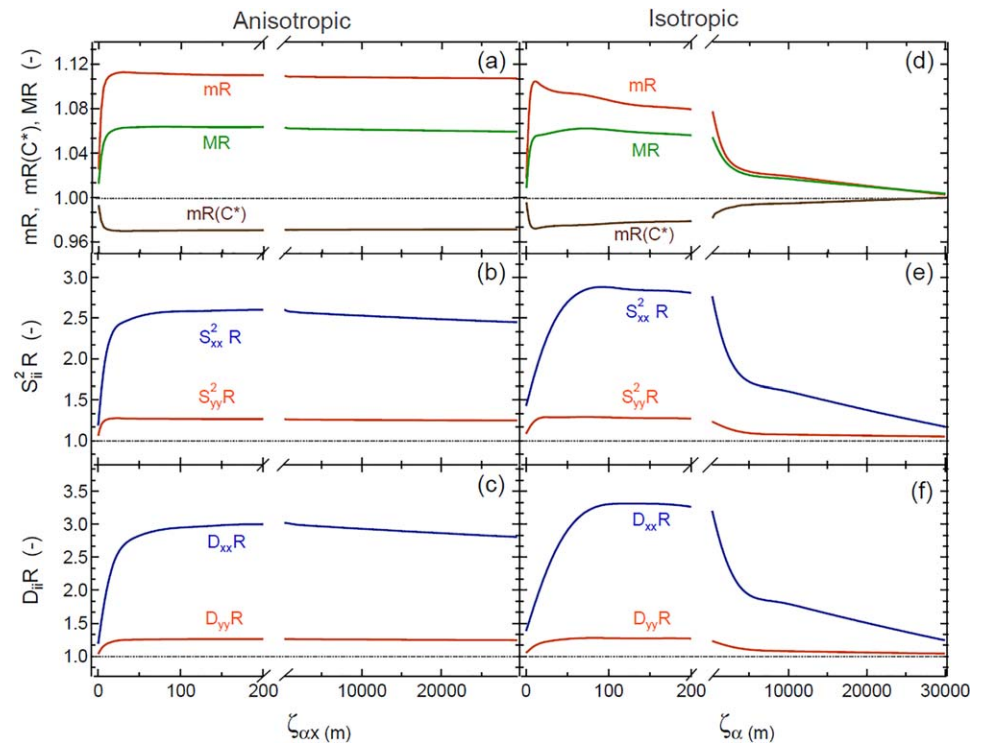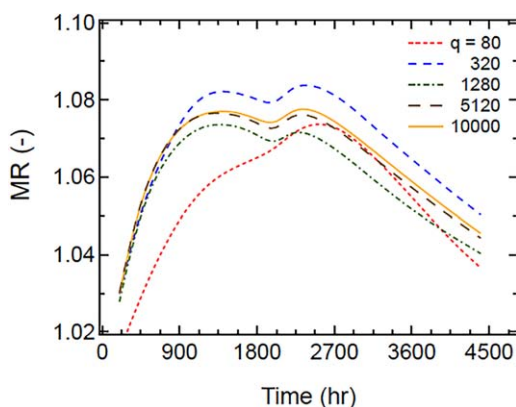
Figure 13. Behavior of the ratios mR, mR(C*), MR, S_{ii}^2R, and $D_{ii}R$ for MS2 migration in the two-dimensional Aquifer-I as a function of: (a-c) the longitudinal correlation length $\zeta_{\alpha x}$ of the anisotropic collision efficiency for $\zeta_{\alpha y}=6$ m, and (d-f) the correlation length ζ_α of the isotropic collision efficiency. Broken x-axes were used for simultaneous and precise presentation of small and big correlation scales. Here $CV=\sigma_\alpha/\mu_\alpha=50\%$, and $t_p>t=600$ h.

based on the Chebyshev inequality (39) and termination criteria II (equation (40)), an acceptable number of runs for the estimation of the MR ratio should be in the range $1,280 < q < 5,120$. Therefore, the use of a randomly selected number of runs for ensemble mean estimation of a stochastic variable can easily lead to erroneous results.

7. Summary and Conclusions

The various effects of spatially variable attachment on biocolloid (i.e. viruses, bacteria) transport in geochemically heterogeneous, structurally homogeneous, water saturated porous media were explored in this work. A numerical transport model was developed assuming that the biocolloid collision efficiency could be described by Gaussian or normally distributed random field. The vital importance of carefully selecting the correct number of runs for the estimation of the ensemble mean of a stochastic variable was reiterated. The results from numerous simulations conducted in two- and three-dimensional porous media revealed that the transport and dispersion of a suspended biocolloid plume was significantly increased at early times with increasing variability and correlation length scale of the biocolloid attachment. The enhanced biocolloid transport was shown to progressively dissipate at late times as the biocolloid plume had sampled all of the geochemical heterogeneity within the porous formation. Increased biocolloid transport and dispersion were also observed in the lateral and vertical directions. Under certain conditions reversible attachment could mask the effects of geochemical heterogeneity. Also, the effects of geochemical heterogeneity were more pronounced with decreasing biocolloid diameter size.

Figure 14. Time history of MR ratio for different number of realizations used, in the two-dimensional anisotropic Aquifer-I. Here $CV=\sigma_\alpha/\mu_\alpha=50\%$, $\zeta_{\alpha x}=15$ m, $\zeta_{\alpha y}=6$ m, and $t_p=2,000$ h.

Unlike previous one-dimensional studies, the three-dimensional analysis presented here investigated temporal effects and explored moments, correlation length, and apparent dispersion. The results clearly suggested that for accurate predictions of biocolloid transport in porous media the aquifer chemical heterogeneity should not be ignored. However, it may be difficult to know precisely the large-scale model parameters that characterize chemical heterogeneity of the collision efficiency (e.g. standard deviation and correlation length). Finally, the main results of this study would not be altered if a different covariance function of the spatially variable collision efficiency was employed.

Nomenclature

A_{123}	Hamaker constant, $M \cdot L^2/t^2$.
A_s	streamline parameter, (–).
A	Dispersivity tensor, defined in (36).
C_b	concentration of suspended biocolloids, M_b/L^3.
C_b^*	concentration of colloids attached onto the solid matrix, M_b/M_s.
Cov_α	covariance function for α, defined in (25).
CV	coefficient of variation, (–).
d_c	collector diameter, L.
d_b	biocolloid particle diameter, L.
D	bulk diffusion coefficient, L^2/t.
D_x	longitudinal hydrodynamic dispersion coefficient, L^2/t.
D_y	lateral hydrodynamic dispersion coefficient, L^2/t.
D_z	vertical hydrodynamic dispersion coefficient, L^2/t.
D	hydrodynamic dispersion tensor, defined in (35).
$D_{ii}R$	ratio of $\langle D_{ii} \rangle$ to $D_{ii}^{(h)}$, (–).
$\langle D_{ii} \rangle$	ensemble mean of the hydrodynamic dispersion coefficient (i=x,y,z), L^2/t.
$D_{ii}^{(h)}$	hydrodynamic dispersion coefficient of the geochemically homogeneous aquifer (i=x,y,z), L^2/t.
$E(\alpha)$	expectation value of α, (–).
$F(C_b^*)$	dynamic blocking function, (–).
F_b	general form of the source configuration, defined in (3), $M_b/L^3 \cdot t$.
F_v	form of the virus source configuration, $M_v/L^3 \cdot t$.
g	gravitational acceleration, L/t^2.
G	mass release function, M_b/t (point source), and $M_b/L^3 \cdot t$ (volume source).
$H(t)$	heaviside or unit step function ($H(t<0)=0$, $H(t \geq 0)=1$), (–).
I	identity matrix.
k	positive real number used in Chebyshev inequality (39), (–).
k_B	Boltzman constant, $M \cdot L^2/(t^2 \cdot T)$.
L	length, L.
L_x	length of porous medium, L.
L_y	width of porous medium, L.
L_z	height of porous medium, L.
m_n^t	absolute temporal moment of n order (n=0,1,2), $t^{n+1} \cdot M_b/L^3$
m_{ijk}^s	three-dimensional absolute spatial moments of order i+j+k (i,j,k=0,1,2), $M_b \cdot L^{i+j+k}$.
$m_{000}^{s-(h)}$	zeroth absolute spatial moment for the geochemically homogeneous aquifer, M_b.
$\langle m_{000}^s \rangle$	ensemble mean of the zeroth absolute spatial moment, M_b.
$m_{000}^{s-(h)}(C*)$	zeroth absolute spatial moment of biocolloids attached onto the solid matrix of the geochemically homogeneous aquifer, M_b/M_s.
$\langle m_{000}^s(C*) \rangle$	ensemble mean of the zeroth absolute spatial moment of biocolloids attached onto the solid matrix, M_b/M_s.
mR	ratio of $\langle m_{000}^s \rangle$ to $m_{000}^{s-(h)}$ (masses are based on C_b), (–).
mR(C*)	ratio of $\langle m_{000}^s \rangle$ to $m_{000}^{s-(h)}$ (masses are based on C_b^*), (–).
M_b	mass of biocolloids, M_b.
M_s	mass of the solid matrix, M_s.
M_v	mass of virus, M_v.

M_w	mass of water, M_w.
M_{mr}	mass release rate, M_b/t (point source), and $M_b/L^3 \cdot t$ (volume source).
M_n^t	normalized temporal moment of n order (n>0), t^n.
M_{ijk}^s	three-dimensional normalized spatial moments, L^{i+j+k}. of order i+j+k (i,j,k=1,2), L^{i+j+k}.
$M_{ijk}^{s-(h)}$	represents the M_{ijk}^s for the geochemically homogeneous aquifer, L^{i+j+k}.
$\langle M_{ijk}^s \rangle$	ensemble mean of M_{ijk}^s, L^{i+j+k}.
$\langle M_{ijk}^s \rangle_q$	ensemble mean of M_{ijk}^s for a given number of q realizations, L^{i+j+k}.
MR	ratio of $\langle M_{100}^s \rangle$ to $M_{100}^{s-(h)}$, (–).
n	order of temporal or spatial moment, (–).
n_i	number of discretization unit cells in the i-direction (i=x,y,z), (–).
N_A	attraction number, (–).
N_g	gravity number, (–).
N_{pe}	Peclet number, (–).
N_R	relative size number, (–).
N_{vdw}	van der Waals number, (–).
q	number of realizations employed, (–).
$\mathbf{r}_\alpha$	vector whose magnitude is the separation distance between two points in space.
$r_{\alpha i}$	separation distance between two points in space in the i-direction (i=x,y,z), L.
r_{b-b*}	rate coefficient of biocolloid attachment onto the solid matrix, 1/t.
r_{b*-b}	rate coefficient of biocolloid detachment from the solid matrix, 1/t.
$\mathbf{S}^2$	spatial covariance tensor, defined in (32).
S_{ij}^2	elements of the spatial covariance tensor (i,j=x,y,z), L^2.
$\langle S_{ij}^2 \rangle$	ensemble mean of the spatial covariance tensor element S_{ii}^2 (i,j=x,y,z), L^2.
$S_{ij}^{2-(h)}$	elements of spatial covariance tensor for the geochemically homogeneous aquifer (i,j=x,y,z), L^2.
$S_{ii}^2 R$	ratio of $\langle S_{ii}^2 \rangle$ to $S_{ii}^{2-(h)}$, (–).
t	time, t.
t_p	source time period, t.
T	temperature, Kelvin.
U_x	interstitial velocity in the x-direction, L/t.
$|\mathbf{U}|$	magnitude of the interstitial velocity vector, (–).
W	characterizes the source geometry, $1/L^3$ (point source), (–) (volume source).
x	Cartesian coordinate in the longitudinal direction, L.
x_i	Cartesian coordinate in the longitudinal direction, of a random point i=1,2, L.
x_0	Cartesian coordinate in the longitudinal direction, of a point source, L.
y	Cartesian coordinate in the lateral direction, L.
y_i	Cartesian coordinate in the lateral direction, of a random point i=1,2, L.
y_0	Cartesian coordinate in the lateral direction, of a point source, L.
z	Cartesian coordinate in the vertical direction, L.
z_0	Cartesian coordinate in the vertical direction, of a point source, L.
z_i	Cartesian coordinate in the vertical direction, of a random point i=1,2, L.

Greek Letters

α	collision efficiency, (–)
ε_θ	porosity dependent parameter, defined in (17), (–)
δ	modified Dirac delta function, 1/L.
Δt	discretization time step, t.
ζ_α	independent of direction correlation length scale, L.
$\zeta_{\alpha i}$	correlation length scale in the i-direction (i=x,y,z), L.
η	single collector removal efficiency, (–).
η_o	single collector removal efficiency for favorable deposition, (–).
θ	porosity, (L^3 voids)/(L^3 solid matrix).
λ_b	decay rate of biocolloids suspended in the liquid phase, 1/t.
λ_b^*	decay rate of biocolloids attached onto the solid matrix, 1/t.
μ	mean value of a generic distribution, (–).
μ_α	average value of the spatially variable biocolloid collision efficiency α, (–).

$\mu_{r_{b-b*}}$	average of the spatially variable rate coefficient of biocolloid attachment onto the solid matrix, 1/t.
$\mu_{r_{b*-b}}$	average of the spatially variable rate coefficient of biocolloid detachment from the solid matrix, 1/t.
μ_w	dynamic viscosity of water, M/(L·t).
$(\mu_M)_q$	rolling sample mean of the first normalized spatial moment in x-direction, equal to $\langle M^s_{100}\rangle_q$, L.
μ_M	ensemble mean of the first normalized spatial moment in x-direction, equal to $\langle M^s_{100}\rangle$, L.
ρ_s	bulk density of the solid matrix, M_s/L^3.
ρ_w	water density M/L^3
σ	standard deviation of a generic distribution, (–).
σ_α	standard deviation of the biocolloid collision efficiency α, (–).
σ_α^2	variance of the biocolloid collision efficiency α, (–).
$(\sigma_M^2)_q$	rolling sample variance of the first normalized spatial moment in x-direction, L^2.
σ_M^2	variance of the first normalized spatial moment in x-direction, L^2.
Φ	filter coefficient, 1/L

References

Abdel-Salam, A., & Chrysikopoulos, C. V. (1995). Modelling of colloid and colloid-facilitated contaminant transport in a two-dimensional fracture with spatially variable aperture. *Transport in Porous Media, 20*, 197–221.

Aris, R. (1956). On the dispersion of a solute in a fluid flowing through a tube. *Proceedings of Royal Society London, Series A, 235*, 67–78.

Bachmann, P. A., Hoggan, D., Kurstak, E., Melnick, J. L., Pereira, H. G., Tattersall, P., & Vago, C. (1979). Parvoviridae: Second report. *Intervirology, 11*(4), 248–254.

Bales, R. C., Hinkle, S. R., Kroeger, T. W., Stockling, K., & Gerba, C. P. (1991). Bacteriophage adsorption during transport through porous media: Chemical perturbations and reversibility. *Environmental Science and Technology, 25*(12), 2088–2095.

Ballio, F., & Guadagnini, A. (2004). Convergence assessment of numerical Monte Carlo simulations in groundwater hydrology. *Water Resour. Res, 40*, W04603. https://doi.org/10.1029/2003WR002876

Bao, W. M. J., Vogler, E. T., & Chrysikopoulos, C. V. (2003). Nonaqueous liquid pool dissolution in three-dimensional heterogeneous subsurface formations. *Environmental Geology, 43*, 968–977.

Bear, J. (1972). *Dynamics of fluids in porous media*. New York: Elsevier.

Bekhit, H. M., & Hassan, A. E. (2005). Stochastic modeling of colloid-contaminant transport in physically and geochemically heterogeneous porous media. *Water Resources Research, 41*, W02010. https://doi.org/10.1029/2004WR003262

Bosma, W. J. P., & van der Zee, S. E. A. T. M. (1993). Transport of reacting solute in a one-dimensional, chemically heterogeneous porous medium. *Water Resources Research, 29*(1), 117–131.

Bradford, S. A., Kim, H., Headd, B., & Torkzaban, S. (2016). Evaluating the transport of bacillus subtilis spores as a potential surrogate for cryptosporidium parvum oocysts. *Environmental Science and Technology, 50*(3), 1295–1303.

Chrysikopoulos, C. V., & Abdel-Salam, A. (1997). Modeling colloid transport and deposition in saturated fractures. *Colloids and Surfaces A: Physicochemical and Engineering Aspects, 121*, 189–202.

Chrysikopoulos, C. V., Kitanidis, P. K., & Roberts, P. V. (1990a). Analysis of one-dimensional solute transport through porous media with spatially variable retardation factor. *Water Resources Research, 26*(3), 437–446.

Chrysikopoulos, C. V., Kitanidis, P. K., & Roberts, P. V. (1992a). Generalized Taylor-Aris moment analysis of the transport of sorbing solutes through porous media with spatially-periodic retardation factor. *Transport in Porous Media, 7*(2), 163–185.

Chrysikopoulos, C. V., Kitanidis, P. K., & Roberts, P. V. (1992b). Macrodispersion of sorbing solutes in heterogeneous porous formations with spatially periodic retardation factor and velocity field. *Water Resources Research, 28*(6), 1517–1529.

Chrysikopoulos, C. V., Roberts, P. V., & Kitanidis, P. K. (1990b). One-dimensional solute transport in porous media with partial well-to-well recirculation: Application to field experiments. *Water Resources Research, 26*(6), 1189–1195. https://doi.org/10.1029/89WR03629

Chrysikopoulos, C. V., & Sim, Y. (1996). One-dimensional virus transport homogeneous porous media with time dependent distribution coefficient. *Journal of Hydrology, 185*, 199–219. https://doi.org/10.1016/0022-1694(95)02990-7

Chrysikopoulos, C. V., & Syngouna, V. I. (2012). Attachment of bacteriophages MS2 and FX174 onto kaolinite and montmorillonite: Extended-DLVO interactions. *Colloids and Surfaces B: Biointerfaces, 92*, 74–83. https://doi.org/10.1016/j.colsurfb.2011.11.028.

Chrysikopoulos, C. V., Syngouna, V. I., Vasiliadou, I. A., & Katzourakis, V. E. (2012). Transport of Pseudomonas putida in a three-dimensional bench scale experimental aquifer, *Transport in Porous Media, 94*, 617–642. https://doi.org/10.1007/s11242-012-0015-z

Deborde, D. C., Woessner, W. W., Kiley, Q. T., & Ball, P. (1999). Rapid transport of viruses in a floodplain aquifer. *Water Research, 33*(10), 2229–2238.

Flynn, M. R., Rossi, P., & Hunkeler, D. (2004). Investigation of virus attenuation mechanisms in a fluvioglacial sand using column experiments. *FEMS Microbiology Ecology, 49*, 89–35.

Freyberg, D. L. (1986). A natural gradient experiment on solute transport in a sand aquifer: 2. Spatial moments and the advection and dispersion of nonreactive tracers. *Water Resources Research, 22*(13), 2031–2046.

Fujita, Y., Ding, W.-H., & Reinhard, M. (1996). Identification of wastewater dissolved organic carbon characteristics in reclaimed wastewater and recharged groundwater. *Water Environmental. Research, 68*, 867–876.

Gao, G., Fu, B., Zhan, H., & Ma, Y. (2013). Contaminant transport in soil with depth-dependent reaction coefficients and time-dependent boundary conditions. *Water Research, 47*, 2507–2522.

Garabedian, S. P. (1987). *Large-scale dispersive transport in aquifers: Field experiments and reactive transport theory* (Ph.D. dissertation). Cambridge, MA: Massachusetts Institute of Technology.

Gerba, C. P. (1984). Applied and theoretical aspects of virus adsorption to surfaces. *Advances in Applied Microbiology 30*, 133–168.

Goltz, M. N., & Roberts, P. V. (1987). Using the method of moments to analyze three-dimensional diffusion-limited solute transport from temporal and spatial perspectives. *Water Resources Research, 23*(8), 1575–1585.

Huysmans, M., & Dassargues, A. (2009). Stochastic analysis of the effect of spatial variability of diffusion parameters on radionuclide transport in a low permeability clay layer. *Hydrogeology Journal, 14*, 1094–1106.

Imai, A., Fukushima, T., Matsuhige, K., Kim, Y.-H., & Choi, K. (2002). Characterization of dissolved organic matter in effluents from wastewater treatment plants. *Water Research*, *36*, 859–870.

James, S. C., & Chrysikopoulos, C. V. (2011). Monodisperse and polydisperse colloid transport in water-saturated fractures with various orientations: Gravity effects. *Advances in Water Resour*, *34*, 1249–1255. h:10.1016/j.advwatres.2011.06.001.

Katzourakis, V. E. (2014). Mathematical modeling of colloid and virus cotransport in porous media. *Advances in Water Resources*, *68*, 62–73. https://doi.org/10.1016/j.advwatres.2014.03.001.2015

Katzourakis, V. E., & Chrysikopoulos, C. V. (2015). Modeling dense-colloid and virus cotransport in three-dimensional porous media. *Journal of Contaminant Hydrology*, *181*, 102–113. h:10.1016/j.jconhyd.2015.05.010.

Kinoshita, T., Bales, R. C., Maguire, K. M., & Gerba, C. P. (1993). Effect of ph on bacteriophage transport through sandy soils. *Journal of Contaminant Hydrology*, *14*, 55–70.

Li, X., Scheibe, T. D., & Johnson, W. P. (2004). Apparent decreases in colloid deposition rate coefficients with distance of transport under unfavorable deposition conditions: A general phenomenon. *Environmental Science and Technology*, *38*(21), 5616–5625.

Loveland, J. P., Bhattacharjee, S., Ryan, J. N., & Elimelech, M. (2003). Colloid transport in a geochemically heterogeneous porous medium: Aquifer tank experiment and modelling. *Journal of Contaminant Hydrology*, *65*, 161–182. h:10.1016/S0169-7722(02)00238-3.

Ma, H., Allen, H. E., & Yin, Y. (2001). Characterization of isolated fractions of dissolved organic matter from natural waters and a wastewater effluent. *Water Research*, *35*, 985–996.

Maghrebi, M., Jankovic, I., Fiori, A., & Dagan, G. (2013). Effective retardation factor for transport of reactive solutes in highly heterogeneous porous formations. *Water Resources Research*, *49*(12), 8600–8604. https://doi.org/10.1002/2013WR014429

Montgomery, D. C., & Runger, G. C. (2013). *Applied statistics and probability for engineers* (p. 279). Hoboken, NJ: John Wiley & Sons, Inc.

Murray, J. P., & Parks, G. A. (1980). Poliovirus adsorption on oxide surfaces: Correspondence with the DLVO-Lifshitz theory of colloid stability. In Kavanaugh, M. C. & Leckie, J. O. (Eds.), *Particulates in water: Characterization, fate, effects and removal, American Chemical Society* (Adv. Chem. Ser., 189, chap. 5, pp 97–133). Washington, DC: American Chemical Society.

Olsen, R. H., Siak, J. S., & Gray, R. H. (1974). Characteristics of PRD1, a plasmid-dependent broad host range DNA bacteriophage. *Journal of Virology*, *14*(3), 689–699.

Papoulis, A. (2002). *Probability, random variables, and stochastic processes* (4th ed., pp. 151). New York, NY: McGraw–Hill.

Pazmino, E., Trauscht, J., & Johnson, W. P. (2014). Release of Colloids from Primary Minimum Contact under Unfavorable Conditions by Perturbations in Ionic Strength and Flow Rate. *Environmental Science and Technology*, *48*(16), 9227–9235.

Pieper, A. P., Ryan, J. N., Amy, R. L., Illangasekare, T. H., & Metge, D. W. (1997). Transport and recovery of bacteriophage PRD1 in a sand and gravel aquifer: Effect of sewage-derived organic matter. *Environmental Science and Technology*, *31*, 1163–1170.

Rajagopalan, R., & Tien, C. (1976). Trajectory analysis of deep-bed filtration with the sphere-in-cell porous media model. *AIChE Journal*, *22*, 523–533.

Redman, J. A., Grant, S. B., Olson, T. M., Hardy, M. E., & Estes, M. K. (1997). Filtration of recombinant Norwalk virus particles and bacteriophage MS2 in quartz sand: Importance of electrostatic interactions. *Environmental Science and Technology*, *31*, 3378–3383.

Ryan, J. N., Elimelech, E., Ard, R. A., Harvey, R. W., & Johnson, P. R. (1999). Bacteriophage PRD1 and silica colloid transport and recovery in an iron oxide-coated sand aquifer. *Environmental Science and Technology*, *33*, 63–73.

Ryan, J. N., & Elimelech, M. (1996). Colloid mobilization and transport in groundwater. *Colloids and Surfaces A: Physicochemical and Engineering Aspects*, *107*, 1–52.

Saiers, J., Hornberger, G. M., & Harvey, C. F. (1994). Colloidal silica transport through structured, heterogeneous media. *Journal of Hydrology*, *163*, 271–288.

Schenk, O., & Gärtner, K. (2004). Solving unsymmetric sparce systems of linear equations with PARADISO. *Journal of Future Generation Computer Systems*, *20*(3), 475–487.

Schijven, J. F., Medema, G. J., Vogelaar, A. J., & Hassanizadeh, S. M. (2000). Removal of microorganisms by deep well injection. *Journal of Contaminant Hydrology*, *44*, 301–327.

Schmidt, V. (2015). *Stochastic geometry, spatial statistics and random fields models and algorithms*. Heidelberg: Springer.

Shamir, U. Y., & Harleman, D. R. F. (1967). Numerical solutions for dispersion in porous mediums. *Water Resources Research*, *3*(2), 557–581.

Sim, Y., & Chrysikopoulos, C. V. (1995). Analytical models for one-dimensional virus transport in saturated porous media. *Water Resources Research*, *31*(5), 1429–1437. https://doi.org/10.1029/95WR00199

Sim, Y., & Chrysikopoulos, C. V. (1998). Three-dimensional analytical models for virus transport in saturated porous media. *Transpory in Porous Med*, *30*, 87–112. https://doi.org/10.1023/A:1006596412177

Sim, Y., & Chrysikopoulos, C. V. (1999). Analytical solutions for solute transport in saturated porous media with semi-infinite or finite thickness. *Advances in Water Resour,ces 22*(5), 507–519. https://doi.org/10.1016/S0309-1708(98)00027-X

Singha, K., & Gorelick, S. M. (2005). Saline tracer visualized with three-dimensional electrical resistivity tomography: Field-scale spatial moment analysis. *Water Resources. Research*, *41*, W05023. https://doi.org/10.1029/2004WR003460

Sun, N., Elimelech, M., Sun, N.-Z., & Ryan, J. N. (2001). A novel two-dimensional model for colloid transport in physically and geochemically heterogeneous porous media. *Journal of Contaminant Hydrology*, *49*, 173–199.

Syngouna, V. I., & Chrysikopoulos, C. V. (2011). Transport of biocolloids in water saturated columns packed with sand: Effect of grain size and pore water velocity. *Journal of Contaminant Hydrology*, *126*, 301–314. https://doi.org/10.1016/j.jconhyd.2011.09.007.

Tufenkji, N., & Elimelech, M. (2004). Correlation equation for predicting single-collector efficiency in physicochemical filtration in saturated porous media. *Environmental Science and Technology*, *38*, 529–536.

Tufenkji, N., & Elimelech, M. (2005). Breakdown of colloid filtration theory: Role of the secondary energy minimum and surface charge heterogeneities. *Langmuir*, *21*(3), 841–852.

Valocchi, A. J. (1989). Spatial moment analysis of the transport of kinetically adsorbing solutes through stratified aquifers. *Water Resources Research*, *25*(2), 273–279.

Vasiliadou, I. A., & Chrysikopoulos, C. V. (2011). Cotransport of *Pseudomonas putida* and kaolinite particles through water saturated columns packed with glass beads. *Water Resources Research*, *47*, W02543. https://doi.org/10.1029/2010WR009560

Walshe, G. E., Pang, L., Flury, M., Close, M. E., & Flintoft, M. (2010). Effects of pH, ionic strength, dissolved organic matter, and flow rate on the cotransport of MS2 bacteriophages with kaolinite in gravel aquifer media. *Water Research*, *44*, 1255–1269.

Yao, K. M., Habibian, M. T., & O'melia, C. R. (1971). Water and waste water filtration: Concepts and applications. *Environmental Sci.enceTechnology*, *5*, 1105–1112.

Yuan, B., Pham, M., & Nguyen, T. H. (2008). Deposition kinetics of bacteriophage MS2 on a silica surface coated with natural organic matter in a radial stagnation point flow cell. *Environmental Science and Technology*, *42*(20), 7628–7633.